

Conservative, high-order particle–mesh scheme with applications to advection-dominated flows

Maljaars, Jakob M.; Labeur, Robert Jan; Trask, Nathaniel; Sulsky, Deborah

DOI

[10.1016/j.cma.2019.01.028](https://doi.org/10.1016/j.cma.2019.01.028)

Publication date

2019

Document Version

Accepted author manuscript

Published in

Computer Methods in Applied Mechanics and Engineering

Citation (APA)

Maljaars, J. M., Labeur, R. J., Trask, N., & Sulsky, D. (2019). Conservative, high-order particle–mesh scheme with applications to advection-dominated flows. *Computer Methods in Applied Mechanics and Engineering*, 348, 443-465. <https://doi.org/10.1016/j.cma.2019.01.028>

Important note

To cite this publication, please use the final published version (if applicable). Please check the document version above.

Copyright

Other than for strictly personal use, it is not permitted to download, forward or distribute the text or part of it, without the consent of the author(s) and/or copyright holder(s), unless the work is under an open content license such as Creative Commons.

Takedown policy

Please contact us and provide details if you believe this document breaches copyrights. We will remove access to the work immediately and investigate your claim.

Conservative, high-order particle-mesh scheme with applications to advection-dominated flows

Jakob M. Maljaars^{a,*}, Robert Jan Labeur^a, Nathaniel Trask^{b,1}, Deborah Sulsky^c

^a*Environmental Fluid Mechanics, Faculty of Civil Engineering and Geosciences, Delft University of Technology, Stevinweg 1, 2600 GA Delft, The Netherlands*

^b*Center for Computing Research, Sandia National Laboratories, Albuquerque, NM 87185-1320, USA*

^c*Department of Mathematics and Statistics, The University of New Mexico, Albuquerque, NM 87131, USA*

Abstract

By combining concepts from particle-in-cell (PIC) and hybridized discontinuous Galerkin (HDG) methods, we present a particle-mesh scheme for flow and transport problems which allows for diffusion-free advection while satisfying mass and momentum conservation - locally and globally - and extending to high-order spatial accuracy. This is achieved via the introduction of a novel particle-mesh projection operator which casts the particle-mesh data transfer as a PDE-constrained optimization problem, permitting advective flux functionals at cell boundaries to be inferred from particle trajectories. This optimization problem seamlessly fits in a HDG framework, whereby the control variables in the optimization problem serve as advective fluxes in the HDG scheme. The resulting algebraic problem can be solved efficiently using static condensation. The performance of the scheme is demonstrated by means of numerical examples for the linear advection-diffusion equation and the incompressible Navier-Stokes equations. The results demonstrate optimal spatial accuracy, and when combined with a θ time integration scheme, second-order temporal accuracy is shown.

Keywords: hybridized discontinuous Galerkin, finite element methods, particle-in-cell, PDE-constrained optimization, conservation, advection-dominated flows

1. Introduction

Advection-dominated flow and transport phenomena arise in many engineering applications, such as the transport and mixing of pollutants, turbulent flows, and multiphase flows including phase transition. Accurate simulation of such problems requires a discretization of the underlying conservation laws with
5 minimal artificial dissipation relative to the physical damping. To this end, numerous numerical methods

*Corresponding author

Email addresses: j.m.maljaars@tudelft.nl (Jakob M. Maljaars), r.j.labeur@tudelft.nl (Robert Jan Labeur), natrask@sandia.gov (Nathaniel Trask), sulsky@math.unm.edu (Deborah Sulsky)

¹Sandia National Laboratories is a multimission laboratory managed and operated by National Technology and Engineering Solutions of Sandia, LLC, a wholly owned subsidiary of Honeywell International, Inc., for the U.S. Department of Energy's National Nuclear Security Administration under contract DE-NA0003525.

have been developed, which may be broadly categorized into Eulerian mesh-based and Lagrangian particle-based schemes.

On one hand, Lagrangian particle-based methods, such as SPH [1], allow for a diffusion-free treatment of advection by transporting a cloud of particles. However, due to the lack of a mesh topology, discretization of the diffusive part in a conservative, yet accurate manner is non-trivial, as pointed out in, e.g., [2, 3, 4, 5]. On the other hand, Eulerian mesh-based methods, such as finite volume (FV) or finite element methods (FEM), use a mesh topology which allows for an efficient discretization of the governing conservation laws, including the constitutive terms. Many of these methods can achieve high-order accuracy, and in particular discontinuous Galerkin (DG) methods (see, e.g., [6, 7] and references) and hybridized discontinuous Galerkin (HDG) methods (see, e.g., [8, 9, 10, 11, 12, 13]) possess attractive local (i.e. cellwise) conservation properties. On the down side, these methods involve diffusive upwinding (e.g., [8, 10, 11, 12, 13]) or other carefully designed formulations (e.g., [9, 14]) to stabilize the discrete advection operator, which may obscure principal features of advection-dominated problems.

By using particles to handle the advective part of a problem and a mesh in the diffusion part, hybrid particle-mesh methods aim to combine the distinct advantages of Lagrangian and Eulerian methods. Tracing back to the 1960s, the particle-in-cell (PIC) method [15] was the first to simultaneously use a set of moving particles and a static mesh successfully, by introducing two auxiliary steps: (1) a projection of the problem variables allocated on particles to the mesh, and (2), an update of particle-based data once the constitutive part has been solved on the mesh. PIC and related methods, such as the material point method (MPM) [16], consider the particles as moving point masses formulating the particle-mesh projections in terms of a summation of particle properties, see, e.g., [17, 18, 19, 20]. While it guarantees conservation of total mass and momentum, this approach has low-order accuracy only [21]. To achieve high-order accuracy, particle-mesh schemes have been proposed in which the particles are considered as moving sampling points of the continuum. Reconstruction of the mesh-based data from the scattered particle data is typically done using moving least squares (MLS) [22, 21] or local ℓ^2 -projections [23], which compromise however exact conservation.

In this work we extend our particle-mesh method presented in [23] by preserving global and local conservation properties on the mesh. The key to the approach is to constrain the particle-mesh projection used in [23] such that the projected field on the mesh lies in the solution space of a mesh-based advection operator corresponding to the particle motion. To this end, the ℓ^2 -projection operator in [23] is augmented with Lagrange-multiplier terms whose control variables can be associated with advective fluxes at cell interfaces. These interface fluxes ensure a conservative adjustment of the cell-wise fields, while the underlying ℓ^2 -projection enforces minimization of the difference between the particle- and mesh-based fields. This new concept couples naturally to an HDG framework, from which it also will inherit the convergence properties. Typical to HDG methods is the formulation of cell-wise balances, where flux boundary conditions for each

cell are imposed via an additional degree-of-freedom at faces (see for instance [8, 9, 10]). This interface field naturally takes on the role of control variable in our constrained ℓ^2 -projection and enables an efficient implementation using static condensation. Owing to this strategy, the proposed scheme may be conceived as an HDG method in which stable advective fluxes are directly inferred from Lagrangian particle motion, thereby avoiding artificial dissipation as typically present in existing (H)DG and FV methods.

The remainder of this work is structured as follows. Section 2 presents a spatiotemporal operator splitting for the advection-diffusion equation, paying attention to the role of the particle-mesh and the mesh-particle projection. In Section 3 we formulate the PDE-constrained particle-mesh projection, and prove consistency and conservation in the semi-discrete setting. For completeness, this section also presents the semi-discrete formulations for the other steps in a particle-mesh scheme. Section 4 presents the corresponding fully-discrete formulations and discusses various algorithmic aspects of the resulting numerical scheme. An extension of the approach to the incompressible Navier-Stokes equations is discussed in Section 5. The performance of the method is assessed for a range of benchmark tests in Section 6, covering pure advection, advection-diffusion and advection-dominated incompressible flows. Conclusions are drawn in Section 7 which also provides an outlook to future research.

2. Problem formulation and definitions

We consider a domain $\Omega \subset \mathbb{R}^d$ (with $d = 2, 3$), having Lipschitz continuous boundary $\Gamma = \partial\Omega$ partitioned into Dirichlet and Neumann boundaries Γ_D and Γ_N , satisfying $\Gamma_D \cup \Gamma_N = \partial\Omega$ and $\Gamma_D \cap \Gamma_N = \emptyset$. The outward pointing unit vector normal to Γ is denoted by \mathbf{n} . The time interval of interest is $I = (t^0, t^N]$, where t^0 and t^N are the start and end time of the simulation.

2.1. Advection-diffusion problem

On the space-time domain $\Omega \times I$, the scalar-valued linear advection-diffusion equation is formulated as a system of two first-order equations as follows: given a solenoidal velocity field $\mathbf{a}: \Omega \times I \rightarrow \mathbb{R}^d$, an initial condition $\phi_0: \Omega \rightarrow \mathbb{R}$, diffusivity κ , and boundary conditions $h: \Gamma_N \times I \rightarrow \mathbb{R}$ and $g: \Gamma_D \times I \rightarrow \mathbb{R}$, find $\phi: \Omega \times I \rightarrow \mathbb{R}$ such that

$$\frac{\partial \phi}{\partial t} + \nabla \cdot \boldsymbol{\sigma} = f \quad \text{in } \Omega \times I, \quad (1a)$$

$$\boldsymbol{\sigma} = \mathbf{a}\phi - \kappa \nabla \phi \quad \text{in } \Omega \times I, \quad (1b)$$

$$\boldsymbol{\sigma} \cdot \mathbf{n} = (1 - \gamma)(\mathbf{a} \cdot \mathbf{n})\phi + h \quad \text{on } \Gamma_N \times I, \quad (1c)$$

$$\phi = g \quad \text{on } \Gamma_D \times I, \quad (1d)$$

$$\phi(\mathbf{x}, t^0) = \phi_0 \quad \text{in } \Omega. \quad (1e)$$

The parameter γ in Eq. (1c) is equal to one at inflow Neumann boundaries (where $\mathbf{a} \cdot \mathbf{n} < 0$) and equal to zero on outflow Neumann boundaries (where $\mathbf{a} \cdot \mathbf{n} \geq 0$), with h specifying the total flux on inflow Neumann boundaries and the diffusive flux on outflow Neumann boundaries.

75 2.2. Operator splitting using projection operators

As in [23], the particle-mesh method is conceived as an operator splitting procedure. To this end, let the time interval of interest I be partitioned using a sequence of $N + 1$ discrete time levels $\{t^0, t^1, \dots, t^{N-1}, t^N\}$ which for $n = 0, N - 1$ defines the half-open subintervals $I_n = (t^n, t^{n+1}]$ such that $\bigcup_n I_n = I$, while $\mathcal{I} := \{I_n\}$ defines the ordered sequence of subintervals. Furthermore, let the total flux given by Eq. (1b) be
80 decomposed additively into an advective part $\boldsymbol{\sigma}_a$ and a diffusive part $\boldsymbol{\sigma}_d$, i.e. $\boldsymbol{\sigma} = \boldsymbol{\sigma}_a + \boldsymbol{\sigma}_d$.

A spatiotemporal operator splitting procedure for the advection-diffusion problem, Eq. (1), now involves a scalar field $\psi : \Omega \times I_n \rightarrow \mathbb{R}$ satisfying an advection problem,

$$\frac{\partial \psi}{\partial t} + \nabla \cdot \boldsymbol{\sigma}_a = 0 \quad \text{in } \Omega \times I_n, \quad (2a)$$

$$\boldsymbol{\sigma}_a = \mathbf{a}\psi \quad \text{in } \Omega \times I_n, \quad (2b)$$

$$85 \quad \boldsymbol{\sigma}_a \cdot \mathbf{n} = (1 - \gamma)(\mathbf{a} \cdot \mathbf{n})\psi + \gamma h_a \quad \text{on } \Gamma_N \times I_n, \quad (2c)$$

$$\psi = g \quad \text{on } \Gamma_D^- \times I_n, \quad (2d)$$

$$\psi(\mathbf{x}, t^n) = \mathcal{P}_L(\phi(\mathbf{x}, t^n)) \quad \text{in } \Omega, \quad (2e)$$

and a scalar field $\phi : \Omega \times I_n \rightarrow \mathbb{R}$ satisfying a diffusion problem,

$$90 \quad \frac{\partial \phi}{\partial t} + \nabla \cdot \boldsymbol{\sigma}_d = f \quad \text{in } \Omega \times I_n, \quad (3a)$$

$$\boldsymbol{\sigma}_d = -\kappa \nabla \phi \quad \text{in } \Omega \times I_n, \quad (3b)$$

$$\boldsymbol{\sigma}_d \cdot \mathbf{n} = h_d \quad \text{on } \Gamma_N \times I_n, \quad (3c)$$

$$\phi = g \quad \text{on } \Gamma_D \times I_n, \quad (3d)$$

$$95 \quad \phi(\mathbf{x}, t^n) = \mathcal{P}_E(\psi(\mathbf{x}, t^{n+1})) \quad \text{in } \Omega. \quad (3e)$$

to be applied sequentially for every $I_n \in \mathcal{I}$. In the advection stage, the Dirichlet boundary condition can only be prescribed at inflow Dirichlet boundaries, denoted with Γ_D^- . The flux prescribed at Γ_N is split into an advective flux h_a and a diffusive flux h_d , such that $h = h_a + h_d$. Note that the advective flux cannot be specified at outflow Neumann boundaries, which is automatically taken care of by virtue of Eq. (2c).
100 Furthermore, \mathcal{P}_L and \mathcal{P}_E are projection operators, which are introduced in order to couple the fields ψ and ϕ , with these fields being naturally defined on the particles and the mesh, respectively.

More precisely, the projection operator \mathcal{P}_L provides the initial condition at t^n from the mesh field to advance the Lagrangian advection problem to t^{n+1} , and the projection operator \mathcal{P}_E provides the initial

condition at t^n from the particle data to advance the Eulerian diffusion problem to t^{n+1} . To remain
 105 consistent with Eq. (1) it is required that $\mathcal{P}_E \circ \mathcal{P}_L$ equals the identity operator.

This paper aims to formulate the projection operators \mathcal{P}_L and \mathcal{P}_E such that exact conservation is
 guaranteed. That is, the projected field ψ satisfies Eq. (2a) in an integral sense over each cell.

2.3. Auxiliary definitions

Let $\mathcal{T} := \{K\}$ denote the triangulation of the domain Ω into open, non-overlapping cells K . A measure
 110 of the cell size is denoted by h_K , and the outward pointing unit normal vector on the boundary ∂K of each
 cell is denoted by \mathbf{n} . The closure of a cell is denoted by $\bar{K} = K \cup \partial K$. Adjacent cells K_i and K_j ($i \neq j$) share
 a common facet $F = \partial K_i \cap \partial K_j$. The set of all facets (including the exterior boundary facets $F = \partial K \cap \partial \Omega$)
 is denoted by \mathcal{F} .

2.3.1. Function spaces

115 The following scalar finite element spaces are defined:

$$W_h := \{w_h \in L^2(\mathcal{T}), w_h|_K \in P_k(K) \forall K \in \mathcal{T}\}, \quad (4)$$

$$T_h := \{\tau_h \in L^2(\mathcal{T}), \tau_h|_K \in P_l(K) \forall K \in \mathcal{T}\}, \quad (5)$$

$$\bar{W}_{h,g} := \{\bar{w}_h \in L^2(\mathcal{F}), \bar{w}_h|_F \in P_k(F) \forall F \in \mathcal{F}, \bar{w}_h = g \text{ on } \Gamma_D\}, \quad (6)$$

120 in which $P(K)$ and $P(F)$ denote the spaces spanned by Lagrange polynomials on K and F , respectively,
 and $k \geq 1$ and $l \geq 0$ indicate the polynomial orders. The space $\bar{W}_{h,g}$ contains single-valued functions
 that are piecewise continuous on facets $F \in \mathcal{F}$. Furthermore, the facet function space $\bar{W}_{h,g}$ satisfies the
 inhomogeneous Dirichlet boundary condition on Γ_D , with the related space $\bar{W}_{h,0}$ satisfying the homogeneous
 Dirichlet boundary condition on Γ_D . Formally, functions in W_h and T_h are only defined at the cell boundary
 125 ∂K via a trace operator, but this technicality is omitted in the sequel to avoid notational clutter.

Anticipating the extension of the scheme to the Navier-Stokes problem in Section 5, \mathbf{W}_h , \mathbf{T}_h , and $\bar{\mathbf{W}}_{h,g}$
 define the finite element spaces of d -vectors in \mathbb{R}^d corresponding to the scalar function spaces W_h , T_h , and
 $\bar{W}_{h,g}$. Function spaces required for the discretization of the pressure terms are defined as

$$Q_h := \{q_h \in L^2(\mathcal{T}), q_h|_K \in P_{k-1}(K) \forall K \in \mathcal{T}\}, \quad (7)$$

$$130 \quad \bar{Q}_h := \{\bar{q}_h \in L^2(\mathcal{F}), \bar{q}_h|_F \in P_k(F) \forall F \in \mathcal{F}\}, \quad (8)$$

where the extension of Q_h to cell boundaries ∂K is assumed implicit in the definition.

2.3.2. Particle definitions

The Lagrangian particle configuration in the domain Ω at a fixed time instant t is defined as follows

$$135 \quad \mathcal{X}_t := \{\mathbf{x}_p(t) \in \Omega\}_{p=1}^{N_p}, \quad (9)$$

in which \mathbf{x}_p denotes the spatial coordinates of particle p and N_p is the number of particles. Furthermore, the index set of all particles and the index set of particles hosted by cell K , at a fixed time instant t are defined as

$$\mathcal{S}_t := \{p \in \mathbb{N} : \mathbf{x}_p(t) \in \mathcal{X}_t\}, \quad (10)$$

$$\mathcal{S}_t^K := \{p \in \mathbb{N} : \mathbf{x}_p(t) \in \overline{K}, \mathbf{x}_p(t) \in \mathcal{X}_t\}. \quad (11)$$

Finally, Lagrangian scalar and vector fields on the particles are defined as,

$$\Psi_t := \{\psi_p(t) \in \mathbb{R}, \forall p \in \mathcal{S}_t\}, \quad (12)$$

$$\mathcal{V}_t := \{\mathbf{v}_p(t) \in \mathbb{R}^d, \forall p \in \mathcal{S}_t\}, \quad (13)$$

where ψ_p and $\mathbf{v}_p(t)$ denote the corresponding scalar and vector quantities associated with particle p .

Importantly, subscripts p and h are used consistently throughout to distinguish between Lagrangian particle data and Eulerian mesh fields, respectively.

3. Semi-discrete formulations

A particle-mesh operator splitting procedure for the advection-diffusion model problem involves the following sequence of steps (see also [23]):

1. *Lagrangian discretization of the advection problem*, in order to solve Eqs. (2a - 2d) at the particle level;
2. *particle-mesh projection*, in order to project the scattered particle data onto a (scalar) field on the Eulerian mesh using the operator $\mathcal{P}_E : \Psi_t \rightarrow W_h$ (see Eq. (3e));
3. *Eulerian discretization of the diffusion equation*, in order to solve Eqs. (3a - 3d) on the mesh;
4. *mesh-particle projection*, in order to update the particle properties from the scalar field on the Eulerian mesh using the operator $\mathcal{P}_L : W_h \rightarrow \Psi_t$ (see Eq. (2e)).

The main endeavour of this paper is twofold: (i) the formulation of a conservative, high-order accurate particle-mesh projection for Step 2, and (ii), the coupling of Step 2 to the other steps such that the overall procedure (Steps 1-4) remains consistent with the strong form of the advection-diffusion problem, Eq. (1). To this end, the various steps of the operator splitting scheme are detailed below, with a particular emphasis on Step 2 in Section 3.2. Consistency will be addressed in Section 3.5.1.

3.1. Lagrangian discretization of the advection problem

The first step, the Lagrangian, particle-based solution of the advection problem Eqs. (2a-2d), is relatively straightforward by decomposing the problem into two ordinary differential equations for the particle scalar

quantity and the particle position. On the time interval I_n , these equations are given by

$$\dot{\psi}_p(t) = 0 \quad \forall p \in \mathcal{S}_t, \quad (14a)$$

$$\dot{\mathbf{x}}_p(t) = \mathbf{a}(\mathbf{x}_p(t), t^n) \quad \forall p \in \mathcal{S}_t, \quad (14b)$$

170 where $\dot{\psi}_p(t)$ and $\dot{\mathbf{x}}_p(t)$ are the total derivatives at time $t \in I_n$ of the scalar quantity and the position of particle p . Furthermore, $\mathbf{a}(\mathbf{x}, t^n)$ is a prescribed solenoidal velocity field at time t^n . An important observation is that ψ_p stays constant throughout the particle advection stage by virtue of Eq. (14a).

3.2. PDE-constrained particle-mesh interaction

The second step involves the projection operator \mathcal{P}_E , transferring the scattered particle data to piecewise
175 continuous fields at the mesh. In [23] this is formulated in terms of a least-squares projections obtained from the following minimization problem

$$\min_{\psi_h \in W_h} J = \sum_{p \in \mathcal{S}_t} \frac{1}{2} (\psi_h(\mathbf{x}_p(t), t) - \psi_p(t))^2. \quad (15)$$

Since W_h is a space of discontinuous functions, Eq. (15) is equivalent to a set of decoupled minimization problems that can be solved efficiently in a cellwise manner. As demonstrated in [23], accurate results are obtained provided that the particle locations satisfy unisolvency with respect to W_h [24]. However, the
180 projection does not guarantee conservation of linear quantities after the sequence of steps of the operator splitting scheme.

To obtain high-order accuracy, the particles are merely used as sampling points of the continuum that, by definition, do not possess a metric to evaluate integral quantities (e.g. mass or momentum) from particle based fields. Conservation properties are therefore lost when projecting fields from the mesh to the particles.
185 One way to preserve these properties is by keeping track of the integral quantities on the mesh. This can be accomplished by constraining the particle-mesh projection to obtain fields ψ_h that satisfy the hyperbolic conservation law, Eq. (2). We therefore augment the functional in Eq. (15) with terms multiplying the hyperbolic conservation law Eq. (2) with a Lagrange multiplier $\lambda_h \in T_h$. Integration by parts leaves an unknown flux on interior cell facets which is formulated in terms of a variable $\bar{\psi}_h \in \bar{W}_{h,g}$, while the
190 Neumann boundary condition Eq. (2c) is substituted on exterior facets. For a given particle field $\psi_p \in \Psi_t$, an advective velocity field $\mathbf{a} : \Omega \times I_n \rightarrow \mathbb{R}^d$, the initial condition $\psi_h^n \in W_h$, and an advective Neumann boundary condition $h_a : \Gamma_N \times I_n \rightarrow \mathbb{R}$, the minimization problem then involves finding the stationary points of the Lagrangian functional

$$\begin{aligned} \mathcal{L}(\psi_h, \bar{\psi}_h, \lambda_h) = & \sum_{p \in \mathcal{S}_t} \frac{1}{2} (\psi_h(\mathbf{x}_p(t), t) - \psi_p(t))^2 + \sum_K \oint_{\partial K} \frac{1}{2} \beta (\bar{\psi}_h - \psi_h)^2 d\Gamma + \int_{\Omega} \frac{\partial \psi_h}{\partial t} \lambda_h d\Omega \\ & - \sum_K \int_K \mathbf{a} \psi_h \cdot \nabla \lambda_h d\Omega + \sum_K \oint_{\partial K \setminus \Gamma_N} \mathbf{a} \cdot \mathbf{n} \bar{\psi}_h \lambda_h d\Gamma + \oint_{\Gamma_N} (1 - \gamma) \mathbf{a} \cdot \mathbf{n} \psi_h \lambda_h d\Gamma + \oint_{\Gamma_N} \gamma h_a \lambda_h d\Gamma, \quad (16) \end{aligned}$$

for every $t \in I_n$. The collection of terms containing λ_h constitutes a weak form of the advection subproblem, Eq. (2). Furthermore, the unknown facet-based field $\bar{\psi}_h \in \bar{W}_{h,g}$ determines the advective flux at interfaces.

200 The additional regularization term containing $\beta > 0$ penalizes the jumps between ψ_h and $\bar{\psi}_h$ on cell interfaces which avoids the problem to become singular in cases with vanishing normal velocity $\mathbf{a} \cdot \mathbf{n}$.

Before proceeding with the derivation of the resulting optimality system, we take a brief moment to interpret the Lagrangian, Eq. (16). First of all, the single-valued facet variable $\bar{\psi}_h \in \bar{W}_{h,g}$ takes on the role of control variable. With this ingredient being provided by the facet fields used in the hybridized
 205 Discontinuous Galerkin (HDG) method, it follows that HDG is a natural choice for imposing the optimality control on the solution. Embedding the optimality system in other, cell-based spatial discretization methods (e.g., finite volumes) is possible as well, however, this would require the definition of an additional interface-based control variable. Second, the optimal solution for ψ_h based on Eq. (16) will in general not minimize the ℓ^2 -error norm, Eq. (15), for the unconstrained and non-conservative case. Indeed, by adding the PDE-
 210 constraint we restrict the minimization of this error to the space of physically admissible functions, i.e., those that satisfy the hyperbolic conservation law. Third, the objective function itself is modified compared to Eq. (15) by adding the regularization term containing β . The influence of this term on the optimal solution is kept small by choosing the parameter β such that the regularization term is small compared to the first term at the right-hand side in Eq. (16).

Equating the variations of Eq. (16) with respect to the three unknowns $(\psi_h, \lambda_h, \bar{\psi}_h) \in (W_h, T_h, \bar{W}_{h,g})$ to zero, results in the following system of variational equations. At time $t \in I_n$, variation with respect to the scalar field ψ_h gives the co-state equation

$$\begin{aligned} & \sum_{p \in \mathcal{S}_t} (\psi_h(\mathbf{x}_p(t), t) - \psi_p(t)) \delta \psi_h(\mathbf{x}_p(t)) - \sum_K \oint_{\partial K} \beta (\bar{\psi}_h - \psi_h) \delta \psi_h d\Gamma \\ & + \int_{\Omega} \frac{\partial \delta \psi_h}{\partial t} \lambda_h d\Omega - \sum_K \int_K \mathbf{a} \cdot \nabla \lambda_h \delta \psi_h d\Omega + \oint_{\Gamma_N} (1 - \gamma) \mathbf{a} \cdot \mathbf{n} \lambda_h \delta \psi_h d\Gamma = 0 \quad \forall \delta \psi_h \in W_h. \end{aligned} \quad (17a)$$

220 Variation with respect to the Lagrange multiplier λ_h gives the state equation,

$$\begin{aligned} & \int_{\Omega} \frac{\partial \psi_h}{\partial t} \delta \lambda_h d\Omega - \sum_K \int_K \mathbf{a} \psi_h \cdot \nabla \delta \lambda_h d\Omega + \sum_K \oint_{\partial K \setminus \Gamma_N} \mathbf{a} \cdot \mathbf{n} \bar{\psi}_h \delta \lambda_h d\Gamma \\ & + \oint_{\Gamma_N} (1 - \gamma) \mathbf{a} \cdot \mathbf{n} \psi_h \delta \lambda_h d\Gamma + \oint_{\Gamma_N} \gamma h_a \delta \lambda_h d\Gamma = 0 \quad \forall \delta \lambda_h \in T_h. \end{aligned} \quad (17b)$$

Finally, variation with respect to the control variable $\bar{\psi}_h$ leads to the optimality condition,

$$\sum_K \oint_{\partial K \setminus \Gamma_N} \mathbf{a} \cdot \mathbf{n} \lambda_h \delta \bar{\psi}_h d\Gamma + \sum_K \oint_{\partial K} \beta (\bar{\psi}_h - \psi_h) \delta \bar{\psi}_h d\Gamma = 0 \quad \forall \delta \bar{\psi}_h \in \bar{W}_{h,0}. \quad (17c)$$

225 After an appropriate discretization of the time derivatives in Eqs. (17a and 17b) - to be discussed in Section 4 - a field $\psi_h \in W_h$ can be reconstructed from the particle data $\psi_p \in \Psi_t$ by solving the optimality system

Eq. (17). This reconstructed field is used to provide the initial condition for the subsequent diffusion subproblem.

3.3. Eulerian discretization of the diffusion equation

230 The discretization of the diffusion step, Eq. (3), is based on the HDG method presented by Labeur & Wells [8] and seeks solutions $(\phi_h, \bar{\phi}_h) \in (W_h, \bar{W}_h)$. This choice allows for trivial projections between fields ψ_h and ϕ_h , which seamlessly fits in the approach used for solving the optimality system Eq. (17). Referring to [8] for further details, the HDG discretization results in a set of local and global problems, stated as: at time $t \in I_n$, given the initial condition $\phi_h^n \in W_h$, the diffusive Neumann boundary condition $h_d : \Gamma_N \rightarrow \mathbb{R}$ and
 235 the diffusivity κ , find $\phi_h \in W_h$ and $\bar{\phi}_h \in \bar{W}_{h,g}$ such that locally

$$\begin{aligned} \int_{\Omega} \frac{\partial \phi_h}{\partial t} w_h d\Omega + \sum_K \int_K \kappa \nabla \phi_h \cdot \nabla w_h d\Omega + \sum_K \oint_{\partial K} \hat{\boldsymbol{\sigma}}_{d,h} \cdot \mathbf{n} w_h d\Gamma \\ + \sum_K \oint_{\partial K} \kappa (\bar{\phi}_h - \phi_h) \mathbf{n} \cdot \nabla w_h d\Gamma = \int_{\Omega} f w_h d\Omega \quad \forall w_h \in W_h, \end{aligned} \quad (18a)$$

and globally

$$\sum_K \oint_{\partial K} \hat{\boldsymbol{\sigma}}_{d,h} \cdot \mathbf{n} \bar{w}_h d\Gamma = \oint_{\Gamma_N} h_d \bar{w}_h d\Gamma \quad \forall \bar{w}_h \in \bar{W}_{h,0}, \quad (18b)$$

240 where $\hat{\boldsymbol{\sigma}}_{d,h}$ is a diffusive flux at cell facets defined by

$$\hat{\boldsymbol{\sigma}}_{d,h} = -\kappa \nabla \phi - \frac{\alpha}{h_K} \kappa (\bar{\phi}_h - \phi_h) \mathbf{n}, \quad (18c)$$

in which α is a dimensionless parameter as is typical to interior penalty methods [25]. Solving Eq. (18) yields $\bar{\phi}_h$ and ϕ_h , where the latter is to be used for updating the particle properties ψ_p in the subsequent
 245 mesh-particle projection step.

3.4. Mesh-particle projection

The mesh-particle projection $\mathcal{P}_L : W_h \rightarrow \Psi_t$ is based on the following minimization problem

$$\min_{\psi_p(t)} J := \sum_{p \in \mathcal{S}_t} \frac{1}{2} (\phi_h(\mathbf{x}_p(t), t) - \psi_p(t))^2, \quad (19)$$

where we emphasize that the objective functional J is also at the basis of the particle-mesh projection
 250 Eq. (16). Carrying out the minimization yields the particularly simple result

$$\psi_p(t) = \phi_h(\mathbf{x}_p(t), t) \quad \forall p \in \mathcal{S}_t. \quad (20)$$

The mesh-particle projection is not restricted to the mapping of the scalar field $\phi_h \in W_h$ itself, but can be applied to project arbitrary fields in W_h - e.g. the temporal increments of ϕ_h , see Section 4.4 - onto the
 255 particles. As such, it is used for updating the particle quantities, which completes the semi-discrete sequence of steps comprising the particle-mesh operator splitting of the advection-diffusion equation.

3.5. Properties of the semi-discrete formulation

We now demonstrate consistency and conservation of the semi-discrete particle-mesh operator splitting method formulated in Eqs. (17), (18) and (20).

260 3.5.1. Consistency

Consistency of the particle-mesh operator splitting scheme entails three different aspects, (i) the operator splitting has to be consistent with the unsplit governing equations (Eqs. (1)), (ii) the Eulerian part of the operator splitting (step 3) has to be consistent with the diffusion subproblem (Eqs. (3)), and (iii), the constraint imposed weakly in the projection operator \mathcal{P}_E (step 2) has to be consistent with the advection
265 subproblem (Eqs. (2)).

To start with (i), splitting of the advection-diffusion equation into a kinematic part (advection problem) and a constitutive part (diffusion equation) has been the subject of numerous studies, and is known to be consistent up to a time step dependent splitting error which vanishes in the continuous time limit, see [26, 27, 28] among many others. However, specific to a particle-mesh framework, we also have to ensure
270 consistency of the projection operators \mathcal{P}_E (particle - mesh) and \mathcal{P}_L (mesh - particle). This implies that in absence of advection the subsequent application of \mathcal{P}_L and \mathcal{P}_E must recover an initially mesh-based field $\psi_h \in W_h$ exactly, which can be expressed mathematically as (see also Section 2.2),

$$\mathcal{P}_E \circ \mathcal{P}_L(\psi_h) = \psi_h \quad \forall \psi_h \in W_h. \quad (21)$$

275 For an arbitrary initial field ψ_h , the mesh-particle projection \mathcal{P}_L formulated in Eq. (20) gives $\psi_p = \psi_h(\mathbf{x}_p)$. By setting $\mathbf{a} = \mathbf{0}$ in the subsequent particle-mesh projection \mathcal{P}_E , and substituting $\psi_p = \psi_h(\mathbf{x}_p)$ in the co-state equation, Eq. (17a), it follows that in the limit $\beta \downarrow 0$ the initial field ψ_h is recovered exactly, while $\lambda_h = 0$ everywhere. This owes to the symmetry in the objective functions underpinning the particle-mesh and the mesh-particle projection for vanishing β , see Eq. (16) and Eq. (19). Since β must be non-zero in
280 order to explicitly couple the state variable ψ_h and the control variable $\bar{\psi}_h$, we choose $\beta > 0$, yet sufficiently small to accurately approximate the consistency criterion on the projection operators.

Concerning (ii), consistency of the HDG method used in the diffusion step was proven in [8]. To prove consistency of the PDE-constrained projection (iii), consider a sufficiently smooth scalar field ψ . Substitution into Eq. (17b) gives, after integration by parts,

$$\begin{aligned} \sum_K \int_{\Omega} \left(\frac{\partial \psi}{\partial t} + \nabla \cdot (\mathbf{a}\psi) \right) \delta \lambda_h d\Omega + \sum_K \oint_{\partial K \setminus \Gamma_N} \mathbf{a} \cdot \mathbf{n} (\bar{\psi}_h - \psi_h) \delta \lambda_h d\Gamma \\ - \oint_{\Gamma_N} \gamma \mathbf{a} \cdot \mathbf{n} \psi \delta \lambda_h d\Gamma + \oint_{\Gamma_N} \gamma h_a \delta \lambda_h d\Gamma = 0 \quad \forall \delta \lambda_h \in T_h, \quad (22) \end{aligned}$$

which demonstrates consistency with the strong form of the advection problem Eqs. (2a-2b) and the Neu-
 290 mann boundary condition Eq. (2c), with the enforcement of $\bar{\psi} = \psi$ on interior cell facets and the Dirichlet
 boundary Γ_D .

3.5.2. Conservation

Since the particles carry point evaluations of the underlying field, lacking a metric to evaluate mass or
 volume, conservation can be satisfied at the mesh level only. The latter requires that the mesh-based parts
 295 of the scheme, i.e. step 4 (diffusion) and step 2 (advection) are both conservative. Since global and local
 conservation of the HDG method for the diffusion step was demonstrated in [8], it remains to prove (mass)
 conservation of the PDE-constrained particle-mesh projection.

Setting $\delta\lambda_h = 1$ in Eq. (17b), and rearranging, leads to

$$\int_{\Omega} \frac{\partial\psi_h}{\partial t} d\Omega = - \sum_K \oint_{\partial K \setminus \Gamma_N} \mathbf{a} \cdot \mathbf{n} \bar{\psi}_h d\Gamma - \oint_{\Gamma_N} (1 - \gamma) \mathbf{a} \cdot \mathbf{n} \psi_h d\Gamma - \oint_{\Gamma_N} \gamma h_a d\Gamma. \quad (23)$$

For a point-wise divergence free vector field \mathbf{a} the boundary integral on the union of interior cell facets
 300 vanishes, due to $\bar{\psi}_h$ being single-valued on facets $F \in \mathcal{F}$. The right-hand side therefore equals the total
 ingoing advective flux at the exterior boundary Γ , thereby proving global mass conservation. For local mass
 conservation, setting $\delta\lambda_h = 1$ on cell K and $\delta\lambda_h = 0$ on $\Omega \setminus K$ gives, after rearrangement,

$$\int_K \frac{\partial\psi_h}{\partial t} d\Omega = - \oint_{\partial K \setminus \Gamma_N} \mathbf{a} \cdot \mathbf{n} \bar{\psi}_h d\Gamma - \oint_{\Gamma_N} (1 - \gamma) \mathbf{a} \cdot \mathbf{n} \psi_h d\Gamma - \oint_{\Gamma_N} \gamma h_a d\Gamma \quad (24)$$

The right-hand side of Eq. (24) constitutes the ingoing advective flux on the cell facet ∂K which proves
 local conservation in terms of the numerical flux on \mathcal{F} .

305 4. Fully-discrete formulations

We now present a fully-discrete formulation of the particle-mesh operator splitting scheme. To this
 end, the time interval of interest I is partitioned using a sequence of $N + 1$ discrete time levels $\{t^0, t^1, \dots,$
 $t^{N-1}, t^N\}$, see also Section 2.2. The particular time stepping strategy we discuss below largely follows the
 approach used in [23], albeit special care is required to render the particle-mesh projection compatible with
 310 the mesh-particle projection.

4.1. Particle advection

From Eq. (14a) it follows that particle quantities other than the position remain constant throughout this
 stage. A fully-discrete implementation of the Lagrangian advection stage is therefore obtained by integrating
 Eq. (14b) in time to advance the particle position from $\mathbf{x}_p^n \rightarrow \mathbf{x}_p^{n+1}$. For this purpose, we use a three-stage
 315 third-order accurate Runge-Kutta scheme.

At inflow boundaries, particles have to enter the domain. To this end, particles are seeded in the cell contiguous to the inflow boundaries, in such a way to keep the number of particles constant in these cells. In order to remain consistent with the boundary conditions in Eq. (2), properties of the inserted particles are interpolated at the intersection point of the particle trajectory with the domain boundary, using the corresponding values imposed by the boundary conditions.

4.2. PDE-constrained particle-mesh projection

The fully-discrete PDE-constrained particle-mesh projection is formulated with the objective to find the optimal scalar field ψ_h at time level $n+1$ given the particle field ψ_p at time t^{n+1} . Employing the θ -method, where $1/2 \leq \theta \leq 1$, the constraint in the Lagrangian functional \mathcal{L} is evaluated at time $t^{n+\theta} := (1-\theta)t^n + \theta t^{n+1}$ using linear interpolation between discrete time levels. To this end, the scalar field ψ_h at time level $n+\theta$ is approximated by

$$\psi_h(t^{n+\theta}) \approx (1-\theta)\psi_h^{*,n} + \theta\psi_h^{n+1} \quad (25)$$

in which $\psi_h^{*,n} \in W_h$ is an initial field given by

$$\psi_h^{*,n} = \psi_h^n + \Delta t_n \left((1-\theta_L)\dot{\phi}_h^{n-1} + \theta_L\dot{\phi}_h^n \right), \quad (26)$$

where $\Delta t_n = t^{n+1} - t^n$ is the time step size, θ_L is an additional time stepping parameter ($1/2 \leq \theta_L \leq 1$, but possibly different from θ), and the increments $\dot{\phi}_h^m$ (with $m = n-1, n$) are defined by

$$\dot{\phi}_h^m = \frac{\phi_h^m - \phi_h^{*,m-1}}{\Delta t_{m-1}}, \quad (27)$$

with ϕ_h^m and $\phi_h^{*,m-1} = \psi_h^{*,m}$ being fields in W_h related to the particular time stepping scheme used in the diffusion problem (step 3) and mesh-particle projection (step 4), see Sections 4.3 and 4.4. The use of $\psi_h^{*,n}$ in Eq. (26) in place of ψ_h^n ensures that the fully-discrete projection operators \mathcal{P}_L and \mathcal{P}_E are mutually consistent, as discussed in Section 3.5.1 and to be elaborated further in Appendix A. The time derivative of the scalar field ψ_h at time level $n+\theta$ is now given by

$$\left. \frac{\partial \psi_h}{\partial t} \right|_{t^{n+\theta}} \approx \frac{\psi_h^{n+1} - \psi_h^{*,n}}{\Delta t_n}, \quad (28)$$

which follows from the linear interpolation used in Eq. (25).

Next, variations of the dependent fields are taken with respect to the degrees of freedom at time level $n+1$, which involves the replacement of variations $(\delta\phi_h, \delta\lambda_h, \delta\bar{\phi}_h) \in (W_h, T_h, \bar{W}_h)$ in the optimality system Eq. (17) with test functions $(w_h, \tau_h, \bar{w}_h) \in (W_h, T_h, \bar{W}_h)$. Using the expression for the time derivative of ψ_h given in Eq. (28), the time derivative appearing in the co-state equation (17a) is approximated as follows

$$\left. \frac{\partial \delta \psi_h}{\partial t} \right|_{t^{n+\theta}} \approx \frac{\delta \psi_h^{n+1} - \delta \psi_h^{*,n}}{\Delta t_n} = \frac{w_h}{\Delta t_n}, \quad (29)$$

since variations $\delta\psi_h^{*,n} \in W_h$ vanish.

345 Given these approximations, the fully-discrete co-state equation reads: given the particle field $\psi_p^n \in \Psi_t$, the particle positions $\mathbf{x}_p^{n+1} \in \mathcal{X}_t$, and the intermediate field $\psi_h^{*,n} \in W_h$, find $(\psi_h^{n+1}, \lambda_h^{n+1}, \bar{\psi}_h^{n+1}) \in (W_h, T_h, \bar{W}_{h,g})$ such that

$$\begin{aligned}
& \sum_{p \in \mathcal{S}_t} (\psi_h^{n+1}(\mathbf{x}_p^{n+1}) - \psi_p^n) w_h(\mathbf{x}_p^{n+1}) - \sum_K \oint_{\partial K} \beta (\bar{\psi}_h^{n+1} - \psi_h^{n+1}) w_h d\Gamma \\
& + \int_{\Omega} \frac{w_h}{\Delta t_n} \lambda_h^{n+1} d\Omega - \theta \sum_K \int_K (\mathbf{a} w_h) \cdot \nabla \lambda_h^{n+1} d\Omega + \theta \oint_{\Gamma_N} (1 - \gamma) \mathbf{a} \cdot \mathbf{n} \lambda_h^{n+1} w_h d\Gamma = 0 \quad \forall w_h \in W_h. \quad (30a)
\end{aligned}$$

Correspondingly, the fully-discrete counterpart of the state equation Eq. (17b) reads:

$$\begin{aligned}
& \int_{\Omega} \frac{\psi_h^{n+1} - \psi_h^{*,n}}{\Delta t_n} \tau_h d\Omega - \theta \sum_K \int_K (\mathbf{a} \psi_h^{n+1}) \cdot \nabla \tau_h d\Omega + \sum_K \oint_{\partial K \setminus \Gamma_N} \mathbf{a} \cdot \mathbf{n} \bar{\psi}_h^{n+1} \tau_h d\Gamma + \theta \oint_{\Gamma_N} (1 - \gamma) \mathbf{a} \cdot \mathbf{n} \psi_h^{n+1} \tau_h d\Gamma \\
& + \oint_{\Gamma_N} \gamma h_a^{n+\theta} \tau_h d\Gamma = (1 - \theta) \sum_K \int_K (\mathbf{a} \psi_h^{*,n}) \cdot \nabla \tau_h d\Omega - (1 - \theta) \oint_{\Gamma_N} (1 - \gamma) \mathbf{a} \cdot \mathbf{n} \psi_h^{*,n} \tau_h d\Gamma \quad \forall \tau_h \in T_h. \quad (30b)
\end{aligned}$$

Finally, the fully-discrete optimality condition becomes

$$\sum_K \oint_{\partial K \setminus \Gamma_N} \mathbf{a} \cdot \mathbf{n} \lambda_h^{n+1} \bar{w}_h d\Gamma + \sum_K \oint_{\partial K} \beta (\bar{\psi}_h^{n+1} - \psi_h^{n+1}) \bar{w}_h d\Gamma = 0 \quad \forall \bar{w}_h \in \bar{W}_{h,0}. \quad (30c)$$

360 In these equations, the Lagrange multiplier λ_h and the control variable $\bar{\psi}_h$ are conveniently taken at time level $n + 1$, which is allowed since these variables are fully-implicit, not requiring differentiation in time.

The reconstructed field ψ_h^{n+1} which is obtained after solving Eq. (30) for $(\psi_h^{n+1}, \lambda_h^{n+1}, \bar{\psi}_h^{n+1})$ will serve as an input to the solver for the diffusion equation.

4.3. Diffusion equation

365 Using a backward Euler time integration as in [23], the fully-discrete counterparts of Eqs. (18) read: given the initial field $\phi_h^{*,n} = \psi_h^{n+1} \in W_h$, the source term f^{n+1} , the diffusive Neumann boundary condition h_d^{n+1} and the diffusivity κ , find $\phi_h^{n+1} \in W_h$ and $\bar{\phi}_h^{n+1} \in \bar{W}_{h,g}$ such that

$$\begin{aligned}
& \int_{\Omega} \frac{\phi_h^{n+1} - \phi_h^{*,n}}{\Delta t_n} w_h d\Omega + \sum_K \int_K \kappa \nabla \phi_h^{n+1} \cdot \nabla w_h d\Omega + \sum_K \oint_{\partial K} \hat{\sigma}_{d,h}^{n+1} \cdot \mathbf{n} w_h d\Gamma \\
& + \sum_K \oint_{\partial K} \kappa (\bar{\phi}_h^{n+1} - \phi_h^{n+1}) \mathbf{n} \cdot \nabla w_h d\Gamma = \int_{\Omega} f^{n+1} w_h d\Omega \quad \forall w_h \in W_h,
\end{aligned} \quad (31a)$$

and

$$\sum_K \oint_{\partial K} \hat{\sigma}_{d,h}^{n+1} \cdot \mathbf{n} \bar{w}_h d\Gamma = \oint_{\Gamma_N} h_d^{n+1} \bar{w}_h d\Gamma \quad \forall \bar{w}_h \in \bar{W}_{h,0}, \quad (31b)$$

in which the fully-discrete diffusive flux $\hat{\sigma}_{d,h}^{n+1}$ is given by

$$\hat{\sigma}_{d,h}^{n+1} = -\kappa \nabla \phi_h^{n+1} - \frac{\alpha}{h_K} \kappa (\bar{\phi}_h^{n+1} - \phi_h^{n+1}). \quad (31c)$$

Solving Eq. (31) for $(\phi_h^{n+1}, \bar{\phi}_h^{n+1})$ provides the ingredients necessary to update the particle field ψ_p in the
 375 subsequent mesh-particle projection step.

4.4. Mesh-particle projection

Finally, a fully-discrete mesh-particle projection is formulated by mapping the increments of the mesh related field (ϕ_h) to the particles using ([23])

$$\psi_p^{n+1} = \psi_p^n + \Delta t_n \left((1 - \theta_L) \dot{\phi}_h^n(\mathbf{x}_p^n) + \theta_L \dot{\phi}_h^{n+1}(\mathbf{x}_p^{n+1}) \right) \quad \forall p \in \mathcal{S}_t, \quad (32)$$

where $1/2 \leq \theta_L \leq 1$, and $\dot{\phi}_h^n \in W_h$ is defined according to Eq. (27). We emphasize the similarity between the formulation for the mesh-particle update (Eq. (32)) and the definition of $\psi_h^{*,n} \in W_h$ in Eq. (26), which is required to respect the consistency condition, Eq. (21), in the fully-discrete setting, see Appendix A. Furthermore, it readily follows that in the advective limit (i.e. for $\kappa = 0$) it holds that $\psi_p^{n+1} = \psi_p^n$, since
 385 $\dot{\phi}_h^n = \dot{\phi}_h^{n+1} = 0$.

4.5. Algorithmic aspects

4.5.1. Choosing the Lagrange multiplier space

A significant simplification of the fully-discrete optimality system is obtained when choosing the polynomial basis for the Lagrange multiplier of the lowest possible order, i.e. $l = 0$. For this particular choice, the
 390 cell integrals in Eqs. (30) containing gradients of the Lagrange multiplier, or of its associated test function, vanish.

This choice will not affect the conservation proofs given by Eqs. (23) and (24). Indeed, for the choice $l = 0$ it readily follows from Eq. (30b) that the cell-integrated temporal increments of the conserved variables remain in balance with the facet fluxes. Except for the outflow Neumann boundaries, these facet fluxes are
 395 implicitly controlled by the interface variable $\bar{\psi}_h^{n+1} \in \bar{W}_{h,g}$, not requiring differentiation in time. Hence, for the presented time integration scheme the major advantage of choosing $l = 0$ is that it avoids time stepping dependencies in the PDE-constrained particle-mesh projection, thus rendering the particle-mesh projection independent of θ . In view of this evident advantage, we will restrict the discussion in the sequel to the choice $l = 0$. In fact, it is only for this particular choice of the Lagrange multiplier space that second-order
 400 accuracy in time can be expected for the given time integration scheme. Furthermore, independent of the choice for l , we expect optimal spatial convergence rates of the scheme of order $k + 1$, provided a sufficiently accurate particle advection scheme is used.

Finally, albeit $l = 0$ is sufficient to guarantee local conservation of linear quantities (e.g. mass and momentum), it is conjectured that conservation of quadratic quantities (e.g. energy) requires $l > 0$. This topic - in combination with alternative time stepping strategies - is left as an interesting area for future investigation.

4.5.2. Accuracy of the time stepping scheme

In [23] - with the particle-mesh projection being formulated in terms of local ℓ^2 -projections - it was shown that overall second-order accuracy in time can be expected when combining a backward Euler method for the Eulerian step, Eq. (31), with a second-order mesh-particle update as in Eq. (32), using $\theta_L = 1/2$. Note that the latter requires saving the particle field from the previous time step. Backward Euler suffices on the Eulerian step since ϕ_h^{n+1} is advanced over one time step from the second-order field $\phi_h^{*,n}$. Thus, the local, second-order accuracy of backward Euler pertains.

To retain this second-order accuracy in time for the PDE-constrained particle-mesh projection pursued here, we have to use $l = 0$ as argued above. In addition, ensuring compatibility between the mesh-particle update, Eq. (32), and the PDE-constrained particle-mesh interaction in the fully-discrete setting, Eq. (30) leads to a definition for $\psi_h^{*,n}$ via Eq. (26). This is further detailed in Appendix A.

4.5.3. Numerical implementation

As is typical for a HDG formulation, the fully-discrete PDE-constrained particle-mesh projections can be implemented efficiently by eliminating the unknowns local to a cell K (i.e. ψ_h^{n+1} and λ_h^{n+1}) in favor of the global control variable $\bar{\psi}_h^{n+1}$ via static condensation. As a result, the size of the global system is reduced significantly as it depends only on the number of degrees of freedom of the control variable. After solving this system for $\bar{\psi}_h^{n+1}$, the local variables ψ_h^{n+1} and λ_h^{n+1} are obtained in a back substitution step.

The global system for the PDE-constrained projection is similar in size to the one resulting from the diffusion equation. Compared to the unconstrained, local ℓ^2 -projection from [23], this indeed is a small price to be paid for obtaining exact conservation.

5. Extension to incompressible Navier-Stokes

The above constrained particle-mesh operator splitting can be extended in a relatively straightforward manner to the incompressible Navier-Stokes equations by using a vector-valued version of the Lagrangian functional, Eq. (16), in order to project the particle specific momenta $\mathbf{v}_p \in \mathcal{V}_t$ onto the mesh (see also the definitions in Section 2.3). Apart from this, the formulation for the Navier-Stokes problem is similar to that for the advection-diffusion problem sharing the same conservation properties. Hence, Lagrangian particles are used for the advection of specific momentum and an Eulerian mesh is used to solve an incompressible, unsteady Stokes problem, where these steps are coupled by the particle-mesh and mesh-particle projections.

435 As in the scalar-valued case, the PDE-constrained particle-mesh projection does not involve upwinding of the interface fluxes. Particular differences occur due to the non-linearity of the advection term and the inclusion of the incompressibility constraint in the diffusive part (Stokes equations):

- The spatial discretization of the unsteady Stokes equations, see Appendix B.3, is based on the HDG formulation as proposed in [29, 13]. As shown in these references, carrying out the discretization using local and global velocity spaces $\mathbf{W}_h, \bar{\mathbf{W}}_{h,g}$, in combination with local and global pressure spaces Q_h, \bar{Q}_h , results in a Stokes solver which is inf – sup stable, conserves momentum globally and locally, is energy stable and produces $H(\text{div})$ -conforming velocity fields $\mathbf{u}_h^{n+1} \in \mathbf{W}_h$.
- The $H(\text{div})$ -conformity of the velocity fields has the distinct advantage in that particles can be advected through velocity fields being pointwise-divergence free within a cell and having a continuous normal component across cell facets, see Appendix B.1. Satisfying these two criteria is paramount in maintaining a uniform particle distribution over time [23].
- The non-linear advection term appearing in the constraint equations, is linearized by using velocity fields explicitly known from the Stokes solve in the previous time step, see Appendix B.2.
- Consistency between the PDE-constrained particle-mesh projection and the mesh-particle projection, requires a definition of the initial velocity field in the PDE-constrained projection as the vector valued counterpart of Eq. (26), see Eq. (B.6).

The fully-discrete formulation of the particle-mesh operator splitting method for the incompressible Navier-Stokes equations is further detailed in Appendix B.

6. Numerical examples

455 In this section, the properties of the proposed method are illustrated for a selection of numerical examples for the linear advection-diffusion equation and the incompressible Navier-Stokes equations. Particular attention is paid to mass and momentum conservation. Throughout, domains $\Omega \in \mathbb{R}^2$ are considered and the time domain of interest is partitioned using constant time step sizes Δt . Furthermore, the regularization term β is set to a fixed value of 10^{-6} for all computations. The penalty parameter α in Eq. (31) (diffusion equation) and Eq. (B.9) (Stokes problem) is set to $12k^2$ and $6k^2$, respectively. Unless otherwise specified, we choose $l = 0$, thus rendering the scheme independent of θ , see Section 4.5.1.

Tools from the finite element framework FEniCS [30] are used to assemble and solve the equations on the mesh arising from the discretization of the PDE-constrained projections, the diffusion equation and the unsteady Stokes equations. A static condensation procedure is applied in all cases and the resulting global systems are solved using direct Gaussian elimination. The computer code for performing the computations is available under an open source license and can be obtained via bitbucket.org/jakob_maljaars/leopart.

6.1. Advection-diffusion: Gaussian hump

The accuracy of the presented method is assessed by considering a (rotating) Gaussian pulse in the diffusive limit, for moderate diffusion, and in the advective limit. The domain of interest is the circular disk $\Omega := \{(x, y) | x^2 + y^2 \leq 0.5\}$ and the velocity field is either set to $\mathbf{a} = \mathbf{0}$ (diffusive limit), or given by

$$\mathbf{a} = \pi (-y, x)^\top. \quad (33)$$

The corresponding analytical solution for a rotating Gaussian pulse is given by

$$\phi(\mathbf{x}, t) = \frac{2\sigma^2}{2\sigma^2 + 4\kappa t} \exp\left(-\frac{\|\bar{\mathbf{x}}(\mathbf{x}, t) - \mathbf{x}_c\|^2}{2\sigma^2 + 4\kappa t}\right), \quad (34)$$

in which $\mathbf{x}_c = (x_c, y_c)^\top$ is the position vector of the center, σ is the initial standard deviation, and κ is a constant diffusivity. Furthermore, $\|\cdot\|^2$ denotes the square of the Euclidean norm and $\bar{\mathbf{x}}(\mathbf{x}, t)$ is a coordinate in the rotating frame of reference, given by $(x \cos(\pi t) + y \sin(\pi t), -x \sin(\pi t) + y \cos(\pi t))^\top$. The initial condition $\phi(\mathbf{x}, 0)$ is deduced from Eq. (34), with the standard deviation σ set to 0.1 and center coordinates $(x_c, y_c) = (-0.15, 0)$. The disk-shaped domain Ω is triangulated using a sequence of mesh refinements, and particles are randomly seeded in Ω such that each cell contains on average 30 particles, initially.

Table 1: Gaussian hump: Overview of model settings for advection-diffusion.

	k	l	θ	θ_L	\mathbf{a}
Case 1	2	0	-	1/2	$\mathbf{0}$
Case 2	1	0	-	1/2	Eq. (33)
Case 3	2	0	-	1/2	Eq. (33)
Case 4	2	1	1/2	1/2	Eq. (33)

Four different cases (listed in Table 1) are considered for three values of the diffusivity, $\kappa = 0.01$, $\kappa = 0.001$, and $\kappa = 0$ (advective limit). The Dirichlet boundary condition for the diffusion step is deduced from the analytical solution Eq. (34), and we emphasize that in the advective limit the particle specific mass ψ_p stays constant by virtue of Eq. (32). The same meshes, initial conditions, and particle distributions are used in all four cases.

Results obtained after a full revolution are presented in Table 2. For Cases 1-3, at least second-order convergence is obtained. More precisely, for the largest value of the diffusivity (i.e. $\kappa = 0.01$), the convergence rate tends to second-order, whereas near-optimal convergence is obtained for moderate diffusion, with diffusivity $\kappa = 0.001$, resulting in third-order convergence for Cases 1 and 3, and second-order convergence for Case 2. In the advective limit, optimal convergence rates are obtained for Cases 2 and 3.

Case 3 and Case 4 only differ in the polynomial orders of the Lagrange multiplier space. However, the convergence rates drastically reduce for Case 4 to approximately second-order for the pure advection test (with $\kappa = 0$) and to approximately first order for the mixed advection-diffusion regime. This behavior illustrates the difference between the choice $l = 0$ compared to $l \geq 1$ in combination with the chosen time stepping scheme, as discussed in Section 4.5.1.

Table 2: Gaussian hump: L^2 -error for advection-diffusion after one full revolution. Convergence rates based on $h_{K,\max}$.

	Mesh			$\kappa = 0.01$		$\kappa = 0.001$		$\kappa = 0.0$	
	Δt	$h_{K,\min}$	$h_{K,\max}$	$\ \phi - \phi_h\ $	Rate	$\ \phi - \phi_h\ $	Rate	$\ \phi - \phi_h\ $	Rate
Case 1	0.08	6.6e-2	1.2e-1	7.3e-5	-	5.3e-4	-	-	
	0.04	3.2e-2	6.2e-2	1.5e-5	2.3	6.0e-5	3.2		
	0.02	1.6e-2	3.1e-2	3.5e-6	2.1	7.5e-6	3.0		
	0.01	7.9e-3	1.6e-2	8.7e-7	2.0	9.6e-7	3.0		
Case 2	0.08	6.6e-2	1.2e-1	1.2e-3	-	7.2e-3	-	1.3e-2	-
	0.04	3.2e-2	6.2e-2	3.3e-4	1.9	1.8e-3	2.0	3.9e-3	1.8
	0.02	1.6e-2	3.1e-2	6.3e-5	2.4	2.7e-4	2.7	9.6e-4	2.0
	0.01	7.9e-3	1.6e-2	1.2e-5	2.4	9.4e-5	1.6	2.4e-4	2.0
Case 3	0.08	6.6e-2	1.2e-1	1.6e-4	-	8.9e-4	-	2.9e-3	-
	0.04	3.2e-2	6.2e-2	1.6e-5	3.3	1.3e-4	2.8	2.5e-4	3.5
	0.02	1.6e-2	3.1e-2	3.0e-6	2.4	1.9e-5	2.8	3.0e-5	3.1
	0.01	7.9e-3	1.6e-2	7.4e-7	2.0	2.4e-6	2.9	4.4e-6	2.8
Case 4	0.08	6.6e-2	1.2e-1	3.2e-3	-	1.4e-2	-	2.8e-2	-
	0.04	3.2e-2	6.2e-2	2.0e-3	0.7	3.4e-3	2.0	1.5e-2	0.9
	0.02	1.6e-2	3.1e-2	1.1e-3	0.9	9.1e-4	1.9	3.1e-3	2.3
	0.01	7.9e-3	1.6e-2	5.6e-4	0.9	5.1e-4	0.8	8.2e-4	1.9

6.2. Advection: rigid body rotation

In order to qualitatively assess the scheme's ability to preserve point and line singularities, we next consider the advection test proposed in [31]. This test comprises the rigid body rotation of a pointy cone (initially centered at $(x, y) = (-0.3, 0)$), a slotted disk (initially centered at $(x, y) = (0, -0.3)$), and a Gaussian hump (initially centered at $(x, y) = (0.15, 0.15)$) on the the circular disk $\Omega := \{(x, y) | x^2 + y^2 \leq 0.5\}$. The velocity field is given by Eq. (33). By virtue of Eq. (32) it follows that in the advective limit the particle specific masses need not be updated, so that any discontinuities at the particle level persist.

A mesh with moderate spatial resolution (Mesh 1, containing 16189 cells), and a fine resolution mesh (Mesh 2, containing 64561 cells) are considered. Approximately 30 particles are assigned per cell initially, resulting in a total number of slightly over 5×10^5 and 2×10^6 particles in total for Mesh 1 and Mesh 2. Time

step sizes are chosen such to keep the CFL-number approximately the same on both meshes, see Table 3.

Table 3: Rigid body rotation: Overview of mesh, particle and time step settings.

	$ \mathcal{T} $	$h_{K,\min}$	$h_{K,\max}$	$ \mathcal{S}_t $	Δt
Mesh 1	16189	7.9e-3	1.6e-2	502480	1e-2
Mesh 2	64561	4.0e-3	7.8e-2	2010783	5e-3

The results obtained for the two different configurations are assessed visually after a half and a full rotation in Fig. 1. Since the particle values are not updated, the initial discontinuities are maintained at the particle level. The shapes of the pointy cone and the Gaussian hump are well-preserved (without numerical damping), both for a half rotation as well as for a full rotation. Although the shape is well-preserved for the slotted-disk, localized overshoot is observed near the discontinuities for a half rotation. Rather than being a dispersion artifact, the over- and undershoot should be interpreted as a resolution issue with the mesh resolution being too coarse to capture the sharp discontinuity at the particle level monotonically. This is clearly illustrated by Fig. 1c and Fig. 1f, showing that the initial condition is accurately recovered for a full rotation at $t = 2$, in contrast to the diffusive results obtained for this test in e.g. [31, 32, 33].

In order to investigate the mass conservation errors, a measure for the relative global mass conservation error at time T is defined as

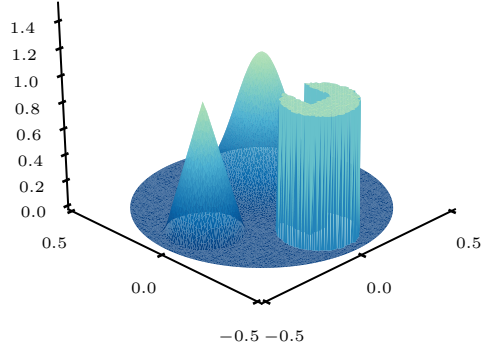
$$\epsilon_{\Delta\phi_\Omega} = \frac{\int_{\Omega} (\phi_h(\mathbf{x}, T) - \phi_h(\mathbf{x}, 0)) d\Omega}{\int_{\Omega} \phi_h(\mathbf{x}, 0) d\Omega}, \quad (35)$$

in which $\phi_h(\mathbf{x}, 0)$ and $\phi_h(\mathbf{x}, T)$ are the mesh related fields at time 0 and time T , respectively.

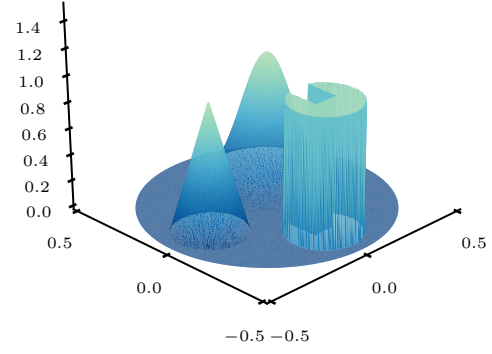
The local mass conservation error is investigated via the L^2 -norm of the time-discrete counterpart of the local conservation statement, Eq. (24). For the problem under consideration, this local mass conservation error norm at time level $n + 1$ is given by

$$\epsilon_{\Delta\phi_K} = \left(\sum_K \left(\int_K \frac{\psi_h^{n+1} - \psi_h^{*,n}}{\Delta t} d\Omega + \oint_{\partial K} \mathbf{a} \cdot \mathbf{n} \bar{\psi}_h^{n+1} d\Gamma \right)^2 \right)^{1/2}. \quad (36)$$

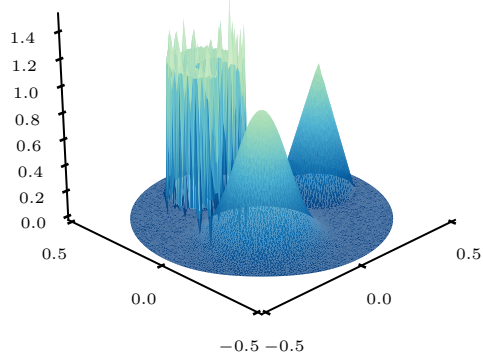
The mass conservation errors as defined by Eqs. (35) and (36) after a half rotation ($T = 1$) and a full rotation ($T = 2$) are tabulated in Table 4, confirming global and local mass conservation of the PDE-constrained projection to machine precision, irrespective of the resolution of the Eulerian mesh.



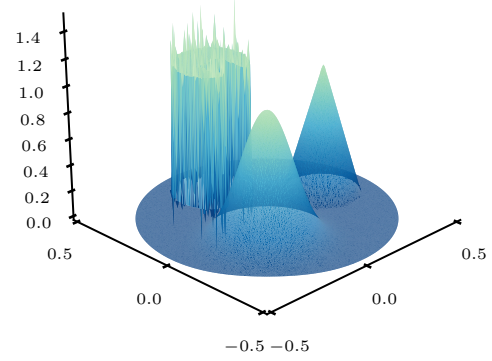
(a) Mesh 1, $t = 0$.



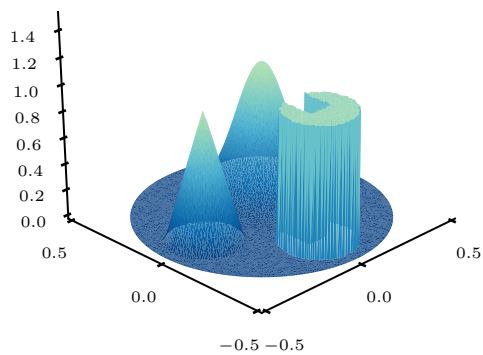
(d) Mesh 2, $t = 0$.



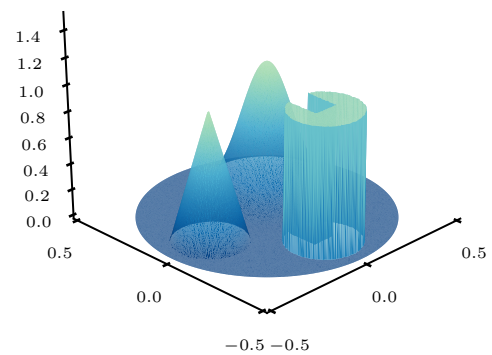
(b) Mesh 1, $t = 1$.



(e) Mesh 2, $t = 1$.



(c) Mesh 1, $t = 2$.



(f) Mesh 2, $t = 2$.

Figure 1: Rigid body rotation: numerical solution ψ_h for different meshes at various time instants using polynomial orders $(k, l) = (1, 0)$.

Table 4: Rigid body rotation: mass conservation errors (defined by Eqs. (35) and (36)) for different mesh configurations after a half rotation ($T = 1$) and a full rotation ($T = 2$).

	Mesh 1		Mesh 2	
	T = 1	T = 2	T = 1	T = 2
$\epsilon_{\Delta\phi_\Omega}$	-2.0e-16	2.0e-16	-3.1e-15	5.9e-16
$\epsilon_{\Delta\phi_K}$	1.7e-16	1.5e-16	1.3e-16	1.3e-16

6.3. Advection: advection skew to mesh

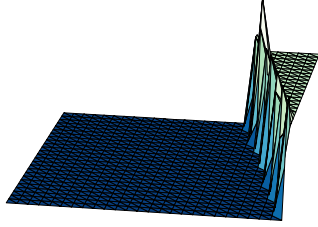
Finally, we consider the advection of a discontinuity on the unit-square $\Omega := [0, 1]^2$ for different transport velocities $\mathbf{u} = [\cos \alpha, \sin \alpha]^\top$ with characteristic directions α of $15^\circ, 30^\circ, 45^\circ, 60^\circ$. The diffusivity κ is set to 0, so that we solve a pure advection problem. A regular triangular mesh is used with uniform cell size $h_K = 1/25$, and each cell contains on average approximately 20 particles. Except for the case $\phi = 45^\circ$, the propagation directions are not aligned with the mesh. Dirichlet boundary conditions are prescribed at the inflow boundaries, and the specific mass ψ_p carried by the particles flowing into the domain is set accordingly. Similar to the preceding rigid body rotation benchmark, the particle specific masses need not be updated, so that any discontinuities at the particle level persist without artificial diffusion. Hence, this test is well-suited for assessing the behavior of the scheme in the presence of steep gradients.

The fields ϕ_h at $t = 2.0$ are plotted in Fig. 2. For a characteristic direction of 45° , the discontinuity is captured exactly at the mesh level. For the other characteristic directions, an overshoot is observed near the discontinuity. However, this overshoot remains strictly localized to one mesh cell upstream of the discontinuity. This behavior can be expected since no attempts are presently made to preserve monotonicity at the mesh, while the discontinuity at the particle level is inherently maintained without any diffusion. We leave the introduction of limiters as a fruitful area for future research, and refer to the work of Bochev and coworkers on bound-preserving remaps as an interesting starting point [32].

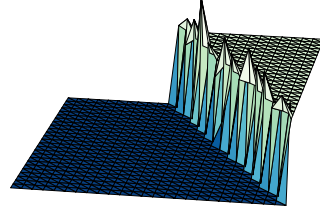
The global mass conservation property of the scheme is verified by virtue of the time-discrete equivalent of Eq. (23). The global mass conservation error, denoted by $\epsilon_{\Delta\phi_\Omega}$, is the residual after subtracting the right-hand side from the left-hand side in this equation. The values for $\epsilon_{\Delta\phi_\Omega}$ thus obtained at $t = 2$ are tabulated in Table 5 for the four characteristic angles, confirming global mass conservation to machine precision.

Table 5: Advection skew to mesh: global mass conservation errors for different characteristic directions.

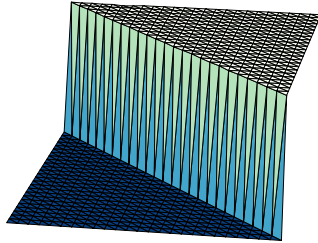
α	15°	30°	45°	60°
$\epsilon_{\Delta\phi_\Omega}$	-1.25e-15	-2.70e-15	-4.43e-15	-4.75e-15



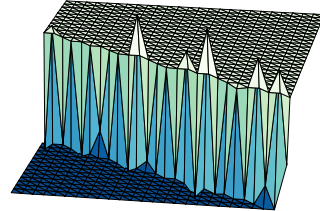
(a) $\alpha = 15^\circ$.



(b) $\alpha = 30^\circ$



(c) $\alpha = 45^\circ$



(d) $\alpha = 60^\circ$

Figure 2: Advection skew to mesh: numerical solution ϕ_h on a unit square domain at $t = 2.0$ for different characteristic directions using polynomial orders $(k, l) = (1, 0)$.

6.4. Navier-Stokes equations: Poiseuille flow

Plane Poiseuille flow is considered to assess the behavior of the particle-mesh operator splitting scheme
 550 for the incompressible Navier-Stokes equations in the presence of no-slip boundaries and to elaborate upon
 the required minimum number of particles per cell.

Starting from rest, the flow gradually develops towards a steady state under the influence of a constant,
 axially applied body force \mathbf{f} . The model domain is given by $\Omega := [0, 1] \times [-0.25, 0.25]$, with the x -axis pointing
 in the flow direction. The flow is periodic in the x -direction and at the location of the plates ($y = \pm 0.25$)
 555 no-flux and no-slip boundary conditions are used in the PDE-constrained particle-mesh projection and the
 Stokes step, respectively. The kinematic viscosity is set to $\nu = 1 \cdot 10^{-3}$, and the body force $\mathbf{f} = (f_x, 0)^T$
 is chosen such that the steady state Reynolds number $Re = 2Ud/\nu$ equals 200. The analytical transient
 solution of the axial velocity can be found in, e.g., [34].

6.4.1. Convergence study

560 The domain of interest Ω is triangulated using a series of refined meshes, and on average, 30 particles are initially assigned per cell. This number is kept constant upon mesh refinement. Throughout, we will use a θ_L -value of $1/2$ for the particle updating, and the time step size corresponds to a CFL-number of approximately 0.25. Results at the dimensionless time instant $t^* = tU/2d = 100$ are presented in Table 6 for polynomial orders $(k, l) = (1, 0)$ and $(k, l) = (2, 0)$. The observed convergence is near-optimal, i.e. order 565 $k + 1$ in the velocity and order k in the pressure.

Table 6: Poiseuille flow: convergence of the L^2 -error in the velocity and the pressure at dimensionless time $t^* = tU/2d = 100$ for different polynomial orders (k, l) .

Cells	Δt	(k,l) = (1, 0)				(k,l) = (2, 0)			
		$\ \mathbf{u} - \mathbf{u}_h\ $	Rate	$\ p - p_h\ $	Rate	$\ \mathbf{u} - \mathbf{u}_h\ $	Rate	$\ p - p_h\ $	Rate
64	0.2	6.2e-3	-	1.4e-4	-	3.9e-6	-	1.3e-7	-
256	0.1	1.6e-3	2.0	8.1e-5	0.7	4.3e-7	3.2	1.8e-8	2.8
1024	0.05	3.9e-4	2.0	3.7e-5	1.2	5.1e-8	3.1	3.7e-9	2.3
4096	0.025	9.7e-5	2.0	1.8e-5	1.0	5.1e-9	3.3	8.0e-10	2.2

6.4.2. Assessing the particle resolution

Evidently, it is desirable from an efficiency perspective to keep the number of particles as low as possible without compromising accuracy. We therefore investigate the influence of the particle resolution on the accuracy by considering the Poiseuille flow benchmark, using $l = 0$ and $k = 1, 2, 3, 4$, combined with a 570 variable particle resolution. We restrict the discussion to the mesh containing 256 cells and a time step of $\Delta t = 0.1$ and only vary the particle resolution for this configuration so that the number of particles per cell (denoted with \bar{S}_0^K) is in the range 2-50, initially. In order to have full control over the initial particle configuration, particles are placed on a regular lattice.

As expected, many of the low particle resolution tests fail prematurely before reaching the end time 575 $t^* = tU/2d = 100$. In Fig. 3, results are visualized by plotting the L^2 -error of the velocity field against the average number of particles per cell for the different polynomial orders. For convenience, we assign an error-value of 1 to all low particle resolution runs failing prematurely.

Evident from the figure is the sharp transition in the error levels. That is, for low particle resolutions the computations are prone to fail prematurely, whereas from a certain particle resolution threshold onward, 580 accurate results are obtained with error values being independent of the particle resolution. Interestingly, this threshold particle resolution depends on the polynomial order of the basis functions and is approximately equal to $\bar{S}_0^K = 8, 8, 10, 15$ for $k = 1, 2, 3, 4$. By recognizing that the particle-mesh projection is based on the local least-squares minimization problem (Eq. (15)), we note that unisolvency of the particle locations with

respect to the discontinuous function space \mathbf{W}_h is a necessary condition for the particle-mesh projection to
 585 be accurate. Empirically, we thus observe this condition to be satisfied if the minimal number of particles
 in a cell is at least equal to the number of local basis functions, except for linear basis functions ($k = 1$) and
 to a lesser extent for quadratic basis functions ($k = 2$), which require a higher number of particles per cell.

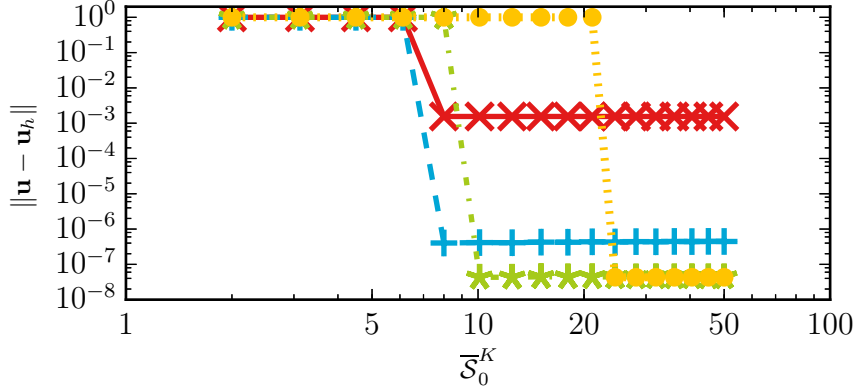


Figure 3: Poiseuille flow: L^2 -error at $t^* = 100$ as a function of the average number of particles initially assigned per cell (\bar{S}_0^K) for an Eulerian mesh with a fixed number of 256 cells and a time step of $\Delta t = 0.1$ for a linear (\times), quadratic ($+$), cubic ($*$) and quartic (\bullet) polynomial basis.

6.5. Navier-Stokes equations: Taylor-Green flow

The Taylor-Green flow on the bi-periodic domain $\Omega := [-1, 1] \times [-1, 1]$ is considered as a final example.
 590 This problem features a periodic sequence of decaying vortices. Provided the Reynolds number is sufficiently
 small, closed analytical expressions for the velocity and the pressure are given by,

$$\mathbf{u}(\mathbf{x}, t) = U \exp(-2\nu\pi^2 t) (-\cos(k_x x) \sin(k_y y), \sin(k_x x) \cos(k_y y))^T, \quad (37)$$

$$p(\mathbf{x}, t) = \frac{1}{4} \exp(-4\nu\pi^2 t) (\cos(2k_x x) + \cos(2k_y y)), \quad (38)$$

595 in which U is the initial velocity amplitude, ν is the kinematic viscosity, and $k_x = 2\pi/L_x$ and $k_y = 2\pi/L_y$
 are wave numbers in the x - and y -direction, with L_x and L_y being the associated wave lengths.

Since body forces and boundary tractions are absent in this test, specific momentum should be conserved.
 In order to verify this, a mesh-related measure for the global momentum conservation error is defined as

$$\epsilon_m = \left| \int_{\Omega} (\mathbf{u}_h(\mathbf{x}, t) - \mathbf{u}_h(\mathbf{x}, 0)) d\Omega \right|. \quad (39)$$

600 To investigate the convergence properties of the scheme, we consider a time interval of interest $I = (0, 2]$.
 The initial peak velocity U in Eq. (37) is set to 1, the wave lengths $L_x = L_y = 2$, and the kinematic
 viscosity is either $\nu = 2 \cdot 10^{-2}$ or $\nu = 2 \cdot 10^{-3}$, with corresponding Reynolds numbers of $Re = UL/\nu = 100$

and $Re = 1000$. The chosen time step corresponds to a CFL-number of approximately 0.4. Different function space combinations are considered, see Table 7. For comparison, Case 3 uses the non-conservative ℓ^2 particle-mesh interaction from [23].

Table 7: Taylor-Green flow: Overview of model settings.

	Projection Method	k	l	θ_L
Case 1	PDE	1	0	1/2
Case 2	PDE	2	0	1/2
Case 3	ℓ^2	2	0	1/2

Table 8: Taylor-Green flow: overview of model runs with the associated errors $\|\mathbf{u} - \mathbf{u}_h\|$, $\|p - p_h\|$ and ϵ_m at time $t = 2$.

			$Re = 100$					$Re = 1000$				
	Cells	Δt	$\ \mathbf{u} - \mathbf{u}_h\ $	Rate	$\ p - p_h\ $	Rate	ϵ_m	$\ \mathbf{u} - \mathbf{u}_h\ $	Rate	$\ p - p_h\ $	Rate	ϵ_m
Case 1	128	0.1	1.2e-1	-	6.5e-2	-	2.8e-15	2.4e-1	-	2.9e-1	-	1.5e-15
	512	0.05	2.4e-2	2.3	2.6e-2	1.3	4.5e-15	4.8e-2	2.3	8.7e-2	1.7	8.1e-15
	2048	0.025	4.7e-3	2.4	1.2e-2	1.1	3.5e-15	1.1e-2	2.1	4.0e-2	1.1	3.6e-15
	8192	0.0125	1.5e-3	1.6	6.0e-3	1.0	1.2e-14	4.0e-3	1.5	2.0e-2	1.0	7.1e-16
Case 2	128	0.1	6.5e-3	-	1.5e-2	-	8.8e-14	7.6e-2	-	5.6e-2	-	1.4e-13
	512	0.05	1.9e-3	1.8	3.2e-3	2.2	1.6e-13	1.2e-2	2.7	1.3e-2	2.1	3.1e-13
	2048	0.025	5.1e-4	1.9	8.4e-3	1.9	3.4e-13	2.3e-3	2.4	3.2e-3	2.0	6.1e-13
	8192	0.0125	1.3e-4	2.0	2.1e-4	2.0	6.3e-13	5.6e-4	2.0	7.8e-4	2.0	1.3e-12
Case 3	128	0.1	6.6e-3	-	1.5e-2	-	3.0e-4	7.6e-2	-	5.6e-2	-	1.3e-3
	512	0.05	1.9e-3	1.8	3.2e-3	2.2	1.2e-4	1.2e-2	2.7	1.3e-2	2.1	6.4e-5
	2048	0.025	5.2e-4	1.9	8.5e-4	1.9	2.9e-6	2.2e-3	2.4	3.1e-3	2.1	1.4e-6
	8192	0.0125	1.3e-4	2.0	2.1e-4	2.0	2.8e-7	5.5e-4	2.0	7.6e-4	2.0	1.5e-6

Velocity and pressure errors are tabulated in Table 8 for different model runs. In all these runs, the average number of particles per cell is 28. For Case 1, consistent second-order convergence is observed for the velocity and first-order convergence is obtained for the pressure. Given the function spaces (piecewise linear velocity, and piecewise constant pressure), no better convergence rates would be expected.

For Case 2, we obtain approximately second-order convergence in the velocity and the pressure, both for the $Re = 100$ test case and the $Re = 1000$ test case. This indicates that the time stepping error becomes dominant over the spatial error, where the former is expected to converge with second-order. Momentum is conserved globally up to machine precision for the PDE-constrained particle-mesh interaction (Case 1, Case 2), whereas this is clearly not so for the unconstrained projection method (Case 3), using local ℓ^2 -projections.

Noteworthy to mention is that the errors in the velocity and pressure are almost identical for Cases 2 and 3.

7. Conclusions and outlook

This paper presented a particle-mesh scheme which allows for diffusion-free advection, satisfies mass and momentum conservation properties in a local (i.e. cellwise) sense, and allows the extension to high-order spatial accuracy. Central in obtaining this, is to formulate the particle-mesh projections in terms of a PDE-constrained minimization problem. The key idea in formulating the constraint is that from a mesh-perspective the particle motion must satisfy a hyperbolic conservation law. By expressing the control variable in terms of single-valued functions at cell interfaces, it was shown that the HDG method naturally provides the necessary ingredients for formulating the optimality system. Consistency and conservation of the constrained interaction were proven. An analysis of the resulting discrete optimality system, revealed that a specific choice for the Lagrange multiplier field renders the PDE-constrained optimization procedure independent of the time integration method, thus resulting in a particularly attractive and robust scheme.

The PDE-constrained particle-mesh interaction is embedded in a Lagrangian-Eulerian operator splitting approach for the advection-diffusion and the incompressible Navier-Stokes equations. Consistency requirements specific to particle-mesh methods were formulated, and a particular fully-discrete formulation was formulated to obey these requirements. A range of numerical experiments unveils the potential of the presented approach. For a pure advection problem the absence of artificial diffusion was confirmed, and standard convergence rates in space and second-order convergence rates in time were confirmed for a range of examples for the linear advection-diffusion problem and the incompressible Navier-Stokes equations. The method turns out to be promising, albeit monotonicity is not guaranteed.

The presented method opens many avenues for further investigation. Future work can include a more rigorous mathematical analysis of the method, finding alternative (high-order time-accurate) operator splitting approaches, and the reconstruction of monotonicity preserving background fields from scattered particle data by, e.g., exploiting the subgrid information available at the particle level. Future work will also investigate the applicability of the presented projection method for mass conservative interface tracking in, e.g., multiphase flows.

Acknowledgements

The Netherlands Organisation for Scientific Research (NWO) is acknowledged for their support through the JMBC-EM Graduate Programme research grant. The first author acknowledges Dr. M. Möller for the useful discussions on the subject, and the 4TU Research Centre FSM for providing travel funding.

N. Trask acknowledges support from the National Science Foundation MSPRF program, the Sandia National Laboratories LDRD program, and from the U.S. Department of Energy Office of Science, Office of

Advanced Scientific Computing Research, Applied Mathematics program as part of the Collaboratory on Mathematics for Mesoscopic Modeling of Materials (CM4).

650 Appendix A. Consistency of the projection operators in the fully-discrete setting

Consider a repeated back-and-forth mapping of a scalar-valued quantity between the particles and the mesh via \mathcal{P}_E and \mathcal{P}_L , while omitting the particle advection step (i.e. $\mathbf{a} = \mathbf{0}$) and the diffusion step (i.e. $\kappa = 0$), and choosing $l = 0$. For ease of presentation, we further assume that the regularization term governed by β is negligibly small as motivated in Section 3.5.1. Consistency in the fully-discrete setting now
655 requires the constraint equations to be inherently satisfied, i.e. $\lambda_h = 0$ everywhere.

To verify this consistency criterion, consider the discrete optimality system Eq. (30) at time level $n + 1$. For a cell K and with $\mathbf{a} = \mathbf{0}$ and $l = 0$, these conditions simplify to

$$\sum_{p \in \mathcal{S}_t^K} \psi_h^{n+1}(\mathbf{x}_p) w_h(\mathbf{x}_p) + \int_K \frac{w_h}{\Delta t} \lambda_h^{n+1} d\Omega = \sum_{p \in \mathcal{S}_t^K} \psi_p^n w_h(\mathbf{x}_p), \quad (\text{A.1a})$$

$$\int_K \frac{\psi_h^{n+1}}{\Delta t} \tau_h d\Omega = \int_K \frac{\psi_h^{*,n}}{\Delta t} \tau_h d\Omega, \quad (\text{A.1b})$$

660

where we used that $\bar{\psi}_h^{n+1}$ and ψ_h^{n+1} coincide in a weak sense over the facets by virtue of the discrete optimality condition for $\mathbf{a} = \mathbf{0}$, Eq. (30c).

With the element contributions following from Eq. (A.1), the system for a single element K can be written
as

665

$$\begin{bmatrix} \mathbf{M}_p & \mathbf{G} \\ \mathbf{G}^\top & \mathbf{0} \end{bmatrix} \begin{bmatrix} \boldsymbol{\psi}_h^{n+1} \\ \boldsymbol{\lambda}_h^{n+1} \end{bmatrix} = \begin{bmatrix} \boldsymbol{\chi}_p \boldsymbol{\psi}_p^n \\ \mathbf{G}^\top \boldsymbol{\psi}_h^{*,n} \end{bmatrix}. \quad (\text{A.2})$$

Performing a Gaussian elimination, results in the following algebraic form for $\boldsymbol{\lambda}^{n+1}$:

$$\mathbf{G}^\top \mathbf{M}_p^{-1} \mathbf{G} \boldsymbol{\lambda}_h^{n+1} = \mathbf{G}^\top (\mathbf{M}_p^{-1} \boldsymbol{\chi}_p \boldsymbol{\psi}_p^n - \boldsymbol{\psi}_h^{*,n}). \quad (\text{A.3})$$

Using the definition of $\boldsymbol{\psi}_h^{*,n}$ in Eq. (26) and updating the particle field $\boldsymbol{\psi}_p^n$ via Eq. (32), it follows that the right hand side of Eq. (A.3) equals zero. Since the mass matrix \mathbf{M}_p is symmetric and non-negative
670 definite [18, 17], the Schur-complement $\mathbf{G}^\top \mathbf{M}_p^{-1} \mathbf{G}$ is non-singular. The solution of Eq. (A.3) is then given by $\boldsymbol{\lambda}_h^{n+1} = \mathbf{0}$ which, after substitution in Eq (A.2), leads to $\boldsymbol{\psi}_h^{n+1} = \mathbf{M}_p^{-1} \boldsymbol{\chi}_p \boldsymbol{\psi}_p^n = \boldsymbol{\psi}_h^{*,n}$. This proves mutual consistency of the operators \mathcal{P}_E and \mathcal{P}_L .

Appendix B. A fully-discrete formulation for the incompressible Navier-Stokes equations

This appendix presents the fully-discrete formulations for the four model components constituting the
675 particle-mesh operator splitting method for the incompressible Navier-Stokes equations. Following [23], such

an operator splitting procedure reads: find a vector-valued field $\mathbf{v} : \Omega \times I_n \rightarrow \mathbb{R}^d$ satisfying an advection problem,

$$\frac{\partial \mathbf{v}}{\partial t} + \nabla \cdot \boldsymbol{\sigma}_a = \mathbf{0} \quad \text{in } \Omega \times I_n, \quad (\text{B.1a})$$

$$\boldsymbol{\sigma}_a = \mathbf{v} \otimes \mathbf{U} \quad \text{in } \Omega \times I_n, \quad (\text{B.1b})$$

$$\boldsymbol{\sigma}_a \mathbf{n} = (1 - \gamma) (\mathbf{v} \otimes \mathbf{U}) \mathbf{n} + \gamma \mathbf{h}_a \quad \text{on } \Gamma_N \times I_n, \quad (\text{B.1c})$$

$$\mathbf{v} = \mathbf{g} \quad \text{on } \Gamma_D^- \times I_n, \quad (\text{B.1d})$$

$$\mathbf{v}(\mathbf{x}, t^n) = \mathcal{P}_L(\mathbf{u}(\mathbf{x}, t^n)) \quad \text{in } \Omega, \quad (\text{B.1e})$$

and a velocity field $\mathbf{u} : \Omega \times I_n \rightarrow \mathbb{R}^d$ satisfying an incompressible Stokes problem,

$$\frac{\partial \mathbf{u}}{\partial t} + \nabla \cdot \boldsymbol{\sigma}_d = \mathbf{f} \quad \text{in } \Omega \times I_n, \quad (\text{B.2a})$$

$$\nabla \cdot \mathbf{u} = 0 \quad \text{in } \Omega \times I_n, \quad (\text{B.2b})$$

$$\boldsymbol{\sigma}_d = p\mathbf{I} - 2\nu\nabla^s \mathbf{u} \quad \text{in } \Omega \times I_n, \quad (\text{B.2c})$$

$$\mathbf{u} = \mathbf{g} \quad \text{on } \Gamma_D \times I_n, \quad (\text{B.2d})$$

$$\boldsymbol{\sigma}_d \mathbf{n} = \mathbf{h}_d \quad \text{on } \Gamma_N \times I_n, \quad (\text{B.2e})$$

$$\mathbf{u}(\mathbf{x}, t^n) = \mathcal{P}_E(\mathbf{v}(\mathbf{x}, t^{n+1})) \quad \text{in } \Omega, \quad (\text{B.2f})$$

with notation similar to Eqs. (2-3). The advective field \mathbf{U} in Eq. (B.1b) is not yet specified, other than to require this field to be a consistent approximation to \mathbf{u} which is piecewise constant on the partitioning \mathcal{I} of the time interval of interest I .

For ease of comparison, the subsection numbering below corresponds to the one used in Section 4.

Appendix B.1. Particle advection

To advect the particle positions, the ODE

$$\dot{\mathbf{x}}_p(t) = \mathbf{U}_h(\mathbf{x}_p(t), t^n) \quad \forall p \in \mathcal{S}_t \quad (\text{B.3})$$

is solved. A judicious choice for the advective field $\mathbf{U}_h(\mathbf{x}, t)$ in this equation is to use the mesh related velocity field $\mathbf{u}_h \in \mathbf{W}_h$, which is obtained in the Stokes step, frozen at the old time level t^n , i.e.

$$\mathbf{U}_h(\mathbf{x}_p(t), t) = \mathbf{u}_h(\mathbf{x}_p(t), t^n). \quad (\text{B.4})$$

The $H(\text{div})$ -conformity of the velocity field $\mathbf{u}_h \in \mathbf{W}_h$ following the solution of the Stokes problem guarantees that the advective field \mathbf{U}_h is pointwise divergence-free [13], while it is also explicitly known in each time interval $I_n \in \mathcal{I}$. Thus, Eq. (B.3) can be integrated in time using explicit integration schemes.

Appendix B.2. PDE-constrained particle-mesh projection

Analogously to Eq. (26), an approximation of the time derivative

$$\frac{\partial \mathbf{v}_h}{\partial t} \Big|_{t^{n+\theta}} \approx \frac{\mathbf{v}_h^{n+1} - \mathbf{v}_h^{*,n}}{\Delta t_n}, \quad (\text{B.5})$$

with $\mathbf{v}_h^{*,n}$ defined as

$$\mathbf{v}_h^{*,n} := \mathbf{v}_h^n + \Delta t_n \left((1 - \theta_L) \dot{\mathbf{u}}^{n-1} + \theta_L \dot{\mathbf{u}}^n \right), \quad (\text{B.6})$$

is used. Furthermore the advective fields are given explicitly by the corresponding velocity fields \mathbf{u}_h and $\bar{\mathbf{u}}_h$ from the previous Stokes step, i.e. for $t \in I_n$ we make use of

$$\mathbf{U}_h(\mathbf{x}, t) := \mathbf{u}_h^n(\mathbf{x}), \quad \text{and} \quad \bar{\mathbf{U}}_h(\mathbf{x}, t) := \bar{\mathbf{u}}_h^n(\mathbf{x}), \quad (\text{B.7})$$

which *de facto* linearizes the PDE-constrained particle-mesh projection problem.

With these definitions, a fully-discrete implementation of the optimality system for the constrained projection of the specific momentum reads: given the vector-valued particle field $\mathbf{v}_p^n \in \mathcal{V}_t$, the particle positions $\mathbf{x}_p^{n+1} \in \mathcal{X}_t$, and the field $\mathbf{v}_h^{*,n} \in \mathbf{W}_h$, and the advective Neumann boundary condition \mathbf{h}_a , find $(\mathbf{v}_h^{n+1}, \boldsymbol{\lambda}_h^{n+1}, \bar{\mathbf{v}}_h^{n+1}) \in (\mathbf{W}_h, \mathbf{T}_h, \bar{\mathbf{W}}_{h,g})$ such that

$$\begin{aligned} & \sum_{p \in \mathcal{S}_t} (\mathbf{v}_h^{n+1}(\mathbf{x}_p^{n+1}) - \mathbf{v}_p^n) \cdot \mathbf{w}_h(\mathbf{x}_p^{n+1}) - \sum_K \oint_{\partial K} \beta (\bar{\mathbf{v}}_h^{n+1} - \mathbf{v}_h^{n+1}) \cdot \mathbf{w}_h d\Gamma + \int_{\Omega} \frac{\mathbf{w}_h}{\Delta t_n} \cdot \boldsymbol{\lambda}_h^{n+1} d\Omega \\ & - \theta \sum_K \int (\mathbf{w}_h \otimes \mathbf{u}_h^n) : \nabla \boldsymbol{\lambda}^{n+1} d\Omega + \theta \oint_{\Gamma_N} (1 - \gamma) (\mathbf{w}_h \otimes \mathbf{u}_h^n) \mathbf{n} \cdot \boldsymbol{\lambda}_h^{n+1} d\Gamma = 0 \quad \forall \mathbf{w}_h \in \mathbf{W}_h. \end{aligned} \quad (\text{B.8a})$$

$$\begin{aligned} & \int_{\Omega} \frac{\mathbf{v}_h^{n+1} - \mathbf{v}_h^{*,n}}{\Delta t_n} \cdot \boldsymbol{\tau}_h d\Omega - \theta \sum_K \int (\mathbf{v}_h^{n+1} \otimes \mathbf{u}_h^n) : \nabla \boldsymbol{\tau}_h d\Omega + \sum_K \oint_{\partial K \setminus \Gamma_N} (\bar{\mathbf{v}}_h^{n+1} \otimes \bar{\mathbf{u}}_h^n) \mathbf{n} \cdot \boldsymbol{\tau}_h d\Gamma \\ & + \theta \oint_{\Gamma_N} (1 - \gamma) (\mathbf{v}_h^{n+1} \otimes \mathbf{u}_h^n) \mathbf{n} \cdot \boldsymbol{\tau}_h d\Gamma + \oint_{\Gamma_N} \gamma \mathbf{h}_a^{n+\theta} \cdot \boldsymbol{\tau}_h d\Gamma \\ & = (1 - \theta) \sum_K \int (\mathbf{v}_h^{*,n} \otimes \mathbf{u}_h^n) : \nabla \boldsymbol{\tau}_h d\Omega - (1 - \theta) \oint_{\Gamma_N} (1 - \gamma) (\mathbf{v}_h^{*,n} \otimes \mathbf{u}_h^n) \mathbf{n} \cdot \boldsymbol{\tau}_h d\Gamma \quad \forall \boldsymbol{\tau}_h \in \mathbf{T}_h, \end{aligned} \quad (\text{B.8b})$$

$$\sum_K \oint_{\partial K \setminus \Gamma_N} (\boldsymbol{\lambda}_h^{n+1} \otimes \mathbf{u}_h^n) \mathbf{n} \cdot \bar{\mathbf{w}}_h d\Gamma + \sum_K \oint_{\partial K} \beta (\bar{\mathbf{v}}_h^{n+1} - \mathbf{v}_h^{n+1}) \cdot \bar{\mathbf{w}}_h d\Gamma = 0 \quad \forall \bar{\mathbf{w}}_h \in \bar{\mathbf{W}}_{h,0}. \quad (\text{B.8c})$$

Solving Eqs. (B.8) for $(\mathbf{v}_h^{n+1}, \boldsymbol{\lambda}_h^{n+1}, \bar{\mathbf{v}}_h^{n+1})$ gives the reconstructed field \mathbf{v}_h^{n+1} , serving as an input to the Stokes solver.

Appendix B.3. Stokes problem

The unsteady Stokes equations are discretized in space employing the HDG formulation from [13, 29]. By using the backward Euler method for the time discretization, the fully-discrete problem reads: given the intermediate field $\mathbf{u}_h^{*,n} = \mathbf{v}_h^{n+1} \in \mathbf{W}_h$, the diffusive Neumann boundary condition $\mathbf{h}_d^{n+1} \in [L^2(\Gamma_N)]^d$, the forcing term $\mathbf{f}^{n+1} \in [L^2(\Omega)]^d$, and the kinematic viscosity ν , find $(\mathbf{u}_h^{n+1}, \bar{\mathbf{u}}_h^{n+1}, p_h^{n+1}, \bar{p}_h^{n+1}) \in (\mathbf{W}_h, \bar{\mathbf{W}}_{h,g}, Q_h, \bar{Q}_h)$ such that (local and global momentum balances),

$$\begin{aligned} \int_{\Omega} \frac{\mathbf{u}_h^{n+1} - \mathbf{u}_h^{*,n}}{\Delta t_n} \cdot \mathbf{w}_h d\Omega - \sum_K \int_K \boldsymbol{\sigma}_{d,h}^{n+1} : \nabla \mathbf{w}_h d\Omega + \sum_K \oint_{\partial K} \hat{\boldsymbol{\sigma}}_{d,h}^{n+1} \mathbf{n} \cdot \mathbf{w}_h d\Gamma \\ + \sum_K \oint_{\partial K} 2\nu (\bar{\mathbf{u}}_h^{n+1} - \mathbf{u}_h^{n+1}) \cdot \nabla^s \mathbf{w}_h \mathbf{n} d\Gamma = \int_{\Omega} \mathbf{f}^{n+1} \cdot \mathbf{w}_h d\Omega \quad \forall \mathbf{w}_h \in \mathbf{W}_h, \end{aligned} \quad (\text{B.9a})$$

$$\sum_K \oint_{\partial K} \hat{\boldsymbol{\sigma}}_{d,h}^{n+1} \mathbf{n} \cdot \bar{\mathbf{w}}_h d\Gamma = \oint_{\Gamma_N} \mathbf{h}_d^{n+1} \cdot \bar{\mathbf{w}}_h d\Gamma \quad \forall \bar{\mathbf{w}}_h \in \bar{\mathbf{W}}_{h,0}, \quad (\text{B.9b})$$

and (local and global mass balances),

$$\sum_K \int_K \mathbf{u}_h^{n+1} \cdot \nabla q_h d\Omega - \sum_K \oint_{\partial K} \mathbf{u}_h^{n+1} \cdot \mathbf{n} q_h d\Gamma = 0 \quad \forall q_h \in Q_h, \quad (\text{B.9c})$$

$$\sum_K \oint_{\partial K} \mathbf{u}_h^{n+1} \cdot \mathbf{n} \bar{q}_h d\Gamma - \oint_{\partial \Omega} \bar{\mathbf{u}}_h^{n+1} \cdot \mathbf{n} \bar{q}_h d\Gamma = 0 \quad \forall \bar{q}_h \in \bar{Q}_h, \quad (\text{B.9d})$$

are satisfied. In these equations, the diffusive fluxes $\boldsymbol{\sigma}_{d,h}^{n+1}$ and $\hat{\boldsymbol{\sigma}}_{d,h}^{n+1}$ are given by

$$\boldsymbol{\sigma}_{d,h}^{n+1} = p_h^{n+1} \mathbf{I} - 2\nu \nabla^s \mathbf{u}_h^{n+1}, \quad (\text{B.10})$$

$$\hat{\boldsymbol{\sigma}}_{d,h}^{n+1} = \bar{p}_h^{n+1} \mathbf{I} - 2\nu \nabla^s \mathbf{u}_h^{n+1} - 2\nu \frac{\alpha}{h_K} (\bar{\mathbf{u}}_h^{n+1} - \mathbf{u}_h^{n+1}) \otimes \mathbf{n}. \quad (\text{B.11})$$

Appendix B.4. Mesh-particle projection

For the incompressible Navier-Stokes equations, the mesh-particle projection is the vector-valued counterpart of Eq. (32), i.e. the momentum field on particles is updated according to

$$\mathbf{v}_p^{n+1} = \mathbf{v}_p^n + \Delta t_n ((1 - \theta_L) \dot{\mathbf{u}}_h^n(\mathbf{x}_p^n) + \theta_L \dot{\mathbf{u}}_h^{n+1}(\mathbf{x}_p^{n+1})) \quad \forall p \in \mathcal{S}_t, \quad (\text{B.12})$$

with $\dot{\mathbf{u}}_h^n(\mathbf{x}_p^n)$ and $\dot{\mathbf{u}}_h^{n+1}(\mathbf{x}_p^{n+1})$ denoting the mesh-based accelerations at the respective time levels n and $n + 1$, evaluated at the individual particle positions.

References

- [1] J. J. Monaghan, Smoothed particle hydrodynamics, Reports Prog. Phys. 68 (8) (2005) 1703–1759. doi:10.1088/0034-4885/68/8/R01.

- [2] G. A. Dilts, A. Haque, J. Wallin, Tuned Local Regression Estimators for the Numerical Solution of Differential Equations, in: *Meshfree Methods for Partial Differential Equations*, Springer, 2003, pp. 87–104. doi:10.1007/978-3-642-56103-0_7.
- 760 [3] L. D. G. Sigalotti, J. Klapp, O. Rendón, C. A. Vargas, F. Peña-Polo, On the kernel and particle consistency in smoothed particle hydrodynamics, *Appl. Numer. Math.* 108 (2016) 242–255. doi:10.1016/J.APNUM.2016.05.007.
- [4] S. J. Lind, P. K. Stansby, High-order Eulerian incompressible smoothed particle hydrodynamics with transition to Lagrangian free-surface motion, *J. Comput. Phys.* 326 (2016) 290–311. doi:10.1016/j.jcp.2016.08.047.
- [5] P. Suchde, J. Kuhnert, S. Schröder, A. Klar, A flux conserving meshfree method for conservation laws, *Int. J. Numer. Methods Eng.* 112 (3) (2017) 238–256. doi:10.1002/nme.5511.
- 765 [6] B. Cockburn, G. E. Karniadakis, C.-W. Shu, The Development of Discontinuous Galerkin Methods, in: *Discontinuous Galerkin Methods*, Springer, Berlin, Heidelberg, 2000, pp. 3–50. doi:10.1007/978-3-642-59721-3_1.
- [7] B. Cockburn, G. Kanschat, D. Schötzau, The local discontinuous Galerkin method for linearized incompressible fluid flow: a review, *Computers & Fluids* 34 (4-5) (2005) 491–506. doi:10.1016/J.COMPFLUID.2003.08.005.
- 770 [8] R. J. Labeur, G. N. Wells, A Galerkin interface stabilisation method for the advection–diffusion and incompressible Navier–Stokes equations, *Comput. Methods Appl. Mech. Eng.* 196 (49) (2007) 4985–5000. doi:10.1016/j.cma.2007.06.025.
- [9] N. Nguyen, J. Peraire, B. Cockburn, An implicit high-order hybridizable discontinuous Galerkin method for linear convection–diffusion equations, *J. Comput. Phys.* 228 (9) (2009) 3232–3254. doi:10.1016/j.jcp.2009.01.030.
- [10] H. Egger, J. Schöberl, A hybrid mixed discontinuous Galerkin finite-element method for convection–diffusion problems, *IMA J. Numer. Anal.* 30 (4) (2010) 1206–1234. doi:10.1093/imanum/drn083.
- 775 [11] R. J. Labeur, G. N. Wells, Energy stable and momentum conserving hybrid finite element method for the incompressible Navier–Stokes equations, *SIAM J. Sci. Comput.* 34 (2) (2012) 889–913. doi:10.1137/100818583.
- [12] C. Lehrenfeld, J. Schöberl, High order exactly divergence-free Hybrid Discontinuous Galerkin Methods for unsteady incompressible flows, *Comput. Methods Appl. Mech. Eng.* 1 307 (2016) 339–361. doi:10.1016/J.CMA.2016.04.025.
- 780 [13] S. Rhebergen, G. N. Wells, A Hybridizable Discontinuous Galerkin Method for the NavierStokes Equations with Pointwise Divergence-Free Velocity Field, *J. Sci. Comput.* (2018) 1–18doi:10.1007/s10915-018-0671-4.
- [14] N. Nguyen, J. Peraire, B. Cockburn, An implicit high-order hybridizable discontinuous Galerkin method for the incompressible NavierStokes equations, *J. Comput. Phys.* 230 (4) (2011) 1147–1170. doi:10.1016/J.JCP.2010.10.032.
- [15] M. Evans, F. Harlow, E. Bromberg, The particle-in-cell method for hydrodynamic calculations, *Tech. rep.*, Los Alamos Scientific Laboratory (1957).
- 785 [16] D. Sulsky, Z. Chen, H. Schreyer, A particle method for history-dependent materials, *Comput. Methods Appl. Mech. Eng.* 118 (1-2) (1994) 179–196. doi:10.1016/0045-7825(94)90112-0.
- [17] J. Brackbill, H. Ruppel, FLIP: A method for adaptively zoned, particle-in-cell calculations of fluid flows in two dimensions, *J. Comput. Phys.* 65 (2) (1986) 314–343. doi:10.1016/0021-9991(86)90211-1.
- 790 [18] D. Burgess, D. Sulsky, J. Brackbill, Mass matrix formulation of the FLIP particle-in-cell method, *J. Comput. Phys.* 103 (1) (1992) 1–15. doi:10.1016/0021-9991(92)90323-Q.
- [19] E. Love, D. Sulsky, An unconditionally stable, energy-momentum consistent implementation of the material-point method, *Comput. Methods Appl. Mech. Eng.* 195 (33-36) (2006) 3903–3925. doi:10.1016/J.CMA.2005.06.027.
- [20] C. Jiang, C. Schroeder, J. Teran, An angular momentum conserving affine-particle-in-cell method, *J. Comput. Phys.* 338 (2017) 137–164. doi:10.1016/J.JCP.2017.02.050.
- 795 [21] D. Sulsky, M. Gong, Improving the Material-Point Method, in: *Innovative Numerical Approaches for Multi-Field and Multi-Scale Problems*, Springer International Publishing, 2016, pp. 217–240. doi:10.1007/978-3-319-39022-2_10.
- [22] E. Edwards, R. Bridson, A high-order accurate particle-in-cell method, *Int. J. Numer. Methods Eng.* 90 (9) (2012) 1073–1088. doi:10.1002/nme.3356.
- 800 [23] J. M. Maljaars, R. J. Labeur, M. Möller, A hybridized discontinuous Galerkin framework for high-order particle–mesh

operator splitting of the incompressible Navier–Stokes equations, *J. Comput. Phys.* 358 (2018) 150–172. doi:10.1016/j.jcp.2017.12.036.

[24] H. Wendland, *Scattered data approximation*, Vol. 17, Cambridge University Press, 2004.

[25] D. N. Arnold, F. Brezzi, B. Cockburn, L. D. Marini, *Unified Analysis of Discontinuous Galerkin Methods for Elliptic Problems*, *SIAM J. Numer. Anal.* 39 (5) (2002) 1749–1779. doi:10.1137/S0036142901384162.

805

[26] G. I. Marchuk, *Splitting and alternating direction methods*, *Handbook of Numerical Analysis 1 (Part I)* (1990) 197–462. doi:10.1016/S1570-8659(05)80035-3.

[27] J. L. Guermond, P. Mineev, J. Shen, *An overview of projection methods for incompressible flows*, *Comput. Methods Appl. Mech. Eng.* 195 (44-47) (2006) 6011–6045. doi:10.1016/j.cma.2005.10.010.

810

[28] J. G. Liu, J. Liu, R. L. Pego, *Stable and accurate pressure approximation for unsteady incompressible viscous flow*, *J. Comput. Phys.* 229 (9) (2010) 3428–3453. doi:10.1016/j.jcp.2010.01.010.

[29] S. Rhebergen, G. N. Wells, *Analysis of a Hybridized/Interface Stabilized Finite Element Method for the Stokes Equations*, *SIAM J. Numer. Anal.* 55 (4) (2017) 1982–2003. doi:10.1137/16M1083839.

[30] A. Logg, K.-A. Mardal, G. N. Wells, *Automated Solution of Differential Equations by the Finite Element Method*, Vol. 84, Springer Science & Business Media, 2012. doi:10.1007/978-3-642-23099-8.

815

[31] R. J. LeVeque, *High-Resolution Conservative Algorithms for Advection in Incompressible Flow*, *SIAM J. Numer. Anal.* 33 (2) (1996) 627–665. doi:10.1137/0733033.

[32] P. Bochev, D. Ridzal, K. Peterson, *Optimization-based remap and transport: A divide and conquer strategy for feature-preserving discretizations*, *J. Comput. Phys.* 257 (2013) 1113–1139. doi:10.1016/j.jcp.2013.03.057.

820

[33] D. Kuzmin, S. Basting, J. N. Shadid, *Linearity-preserving monotone local projection stabilization schemes for continuous finite elements*, *Comput. Methods Appl. Mech. Eng.* 322 (2017) 23–41. doi:10.1016/J.CMA.2017.04.030.

[34] L. D. G. Sigalotti, J. Klapp, E. Sira, Y. Meleán, A. Hasmy, *SPH simulations of time-dependent Poiseuille flow at low Reynolds numbers*, *J. Comput. Phys.* 191 (2) (2003) 622–638. doi:10.1016/S0021-9991(03)00343-7.